NEUROSCIENCE

Numb regulates Tau levels and prevents neurodegeneration in tauopathy mouse models

Marine Lacomme[1], Sarah C. Hales[1,2], Thomas W. Brown[1,2], Katarina Stevanovic[1], Christine Jolicoeur[1], Jenny Cai[1], Therence Bois[1], Melissa Desrosiers[3], Deniz Dalkara[3], Michel Cayouette[1,2,4,5]*

Copyright © 2022 The Authors, some rights reserved; exclusive licensee American Association for the Advancement of Science. No claim to original U.S. Government Works. Distributed under a Creative Commons Attribution NonCommercial License 4.0 (CC BY-NC).

Accumulation of the microtubule-associated protein Tau is linked to neuronal cell death in tauopathies, but how intraneuronal Tau levels are regulated in health and disease remains unclear. Here, we show that conditional inactivation of the trafficking adaptor protein Numb in retinal ganglion cells (RGCs) increases Tau levels and leads to axonal blebbing, which is followed by neuronal cell loss in aged mice. In the TauP301S mouse model of tauopathy, conditional inactivation of Numb in RGCs and spinal motoneurons accelerates neurodegeneration, and loss of Numb in motoneurons also leads to precocious hindlimb paralysis. Conversely, overexpression of the long isoform of Numb (Numb-72) decreases intracellular Tau levels and reduces axonal blebbing in TauP301S RGCs, leading to improved electrical activity in cultured neurons and improves performance in a visually guided behavior test in vivo. These results uncover Numb as a key regulator of intracellular Tau levels and identify Numb-72 as a potential therapeutic factor for tauopathies.

INTRODUCTION

The microtubule binding protein Tau is a soluble protein generally thought to stabilize axonal microtubules in healthy neurons, but recent work more specifically showed that Tau promotes the assembly of long labile domain axonal microtubules (*1*). In a group of neurodegenerative diseases called tauopathies, posttranslational modifications generate insoluble Tau, which can lead to the formation of toxic oligomers and neurofibrillary tangles (*2*–*4*). In recent years, accumulation of Tau oligomers has been shown to contribute directly to neurodegeneration (*5*–*7*), leading to the idea that lowering intracellular levels of Tau before it forms oligomers might alleviate the toxic effects of these oligomers and prevent neuronal cell death in tauopathies. However, would decreasing the levels of native Tau proteins produce undesirable effects? Unexpectedly, inactivation of *Mapt*, the gene coding for Tau, is relatively well tolerated in mice (*8*, *9*), suggesting that Tau-lowering approaches may be viable. Accordingly, reducing Tau protein levels in various ways—such as via antisense oligonucleotides, stimulation of proteasomal degradation and autophagy, or manipulation of a kinase regulating Tau stability—was found to prevent or even reverse neurological phenotypes in tauopathy human neurons and mouse models (*10*–*13*). While these studies demonstrate the therapeutic potential of Tau-lowering approaches, how Tau levels are exactly normally regulated at steady state remains largely unclear. Therefore, we aimed to identify natural regulators of Tau trafficking, which we postulated would not only advance our understanding of how Tau levels are regulated in healthy neurons and how it might become dysregulated in disease but also provide unprecedented ways to lower Tau levels and protect neurons in tauopathy.

Regulation of intracellular trafficking plays a critical part in protein homeostasis. One adaptor protein that was found to regulate intracellular trafficking in the nervous system is Numb. In Drosophila sensory organ precursors, d-numb regulates cell fate decisions by decreasing Notch signaling (*14*). In vertebrates, Numb and Numb-like (Nbl) are homologs of d-numb and display extensive sequence homology and functional redundancy, including inhibition of Notch signaling via ubiquitination of the Notch receptor and trafficking of the intracellular domain for proteasome-mediated degradation (*15*, *16*). Numb and Nbl were also found to play an important role in cell fate decisions during neural progenitor asymmetric divisions (*17*), neuronal migration (*18*), neurite outgrowth (*19*, *20*), and axon guidance (*21*). Classically referred to as an antagonist of Notch signaling, Numb has since been involved in the trafficking of many different cargo proteins (*22*, *23*). Alternative splicing of Numb leads to the production of four different isoforms in mice, defined by their short or long phosphotyrosine-binding domain (PTB) and proline-rich region (PRR), which are thought to mediate different functions. A previous study showed that Numb isoforms with a short PTB (Numb-65 and Numb-71) are elevated in the parietal cortex of patients with Alzheimer's (*24*), suggesting that a correct balance between the long (Numb-72 and Numb-66) and short PTB isoforms may play a role in neuronal survival. However, while Numb function has been extensively studied in various neurodevelopmental contexts, its role in mature neurons remains largely unexplored. Given the widespread expression of Numb in the adult central nervous system (CNS) and its role in intracellular trafficking, we hypothesized that it may be involved in regulating Tau homeostasis, thereby promoting neuronal survival.

To test this hypothesis, we primarily used the mouse retina as a model system. In Alzheimer's disease and other tauopathies, retinal ganglion cells (RGCs), the projection neurons of the retina, display elevated Tau levels and eventually degenerate (*25*–*28*). Consistently, Tau overexpression in mouse RGCs triggers cell death (*29*, *30*), and mouse models of tauopathy display RGC degeneration (*27*, *31*). Therefore, similar to brain neurons, RGCs are highly sensitive to an increase in Tau levels. Combined with the accessibility and anatomical simplicity of the mouse retina, this makes RGCs particularly attractive

[1]Cellular Neurobiology Research Unit, Institut de recherches cliniques de Montréal (IRCM), Montreal, QC H2W 1R7, Canada. [2]Integrated Program in Neuroscience, McGill University, Montreal, QC, Canada. [3]Sorbonne Université, INSERM, CNRS, Institut de la Vision, 17 rue Moreau, F-75012 Paris, France. [4]Department of Medicine, Université de Montréal, Montreal, QC H3T 1J4, Canada. [5]Department of Anatomy and Cell Biology, Division of Experimental Medicine, McGill University, Montreal, QC H3A 0G4, Canada.
*Corresponding author. Email: michel.cayouette@ircm.qc.ca

to study the role of Numb in the regulation of Tau in CNS neurons. Using conditional mouse genetics and tauopathy disease models, we report here that Numb is an essential regulator of intraneuronal Tau levels and prevents degeneration of tauopathy neurons in an isoform-specific manner.

RESULTS

Numb is required for long-term neuronal survival

We previously reported that *Numb* and *Nbl* transcripts are both expressed in the RGC layer of the adult mouse retina (*32*). As the RGC layer also contains displaced amacrine cells and astrocytes, we first sought to determine more precisely whether Numb and Nbl proteins are actually expressed in RGCs by costaining adult retinal sections for Brn3b, a pan-RGC marker, together with an antibody that recognizes both Numb and Nbl (fig. S1, A to C) (*33*). As expected, Numb/Nbl were detected in RGCs, including their axons and dendrites, although the strongest signal was observed in the soma (fig. S1, D and E).

To uncover a potential role for Numb/Nbl in RGCs, we crossed the Islet1-Cre driver mouse line (*34*) to the Numb-floxed line, in which exon 1 of the *Numb* gene is flanked by loxP sites (*35*). As *Nbl* is known to compensate for the loss of *Numb* in multiple contexts (*36*), we generated the *Numb* conditional knockout mouse on an *Nbl* null background (*37*), allowing us to study the specific role of *Numb* in RGCs (fig. S1F). To assess Cre activity, we additionally introduced a Rosa26-loxP-STOP-loxP–tdTomato (tdT) reporter allele. As expected, tdT expression was observed in Islet1-expressing cells in the retina, such as RGCs, from as early as embryonic day 14.5, as well as bipolar cells and a subset of amacrine cells (fig. S1, G to L) (*38*). In this study, Islet1$^{Cre/+}$; Numb$^{fl/fl}$; Numbl$^{del/del}$ animals will be referred to as conditional double knockouts (cDKOs), Islet1$^{Cre/+}$; Numb$^{fl/+}$; Numbl$^{del/del}$ will be referred to as Numb$^{+/-}$;Nbl KO and Islet1$^{+/+}$, and Numb$^{fl/fl}$; Numbl$^{del/del}$ will be referred as Nbl KO. As expected, we found a loss of Numb immunostaining signal in cDKO RGCs compared to Numb$^{+/-}$; Nbl KO (fig. S1, M to P). As Nbl is null in both conditions, we conclude that the immunostaining signal observed in RGCs is specific for Numb. We also performed polymerase chain reaction (PCR) on genomic DNA of adult retinas from wild type (WT), Numb$^{+/-}$; Nbl KO, Nbl KO, and cDKO (fig. S1, Q to T). The excision was not complete, but this was expected because a large proportion of cells expressing Numb in the retina do not carry the Islet-Cre driver. These results confirm the generation of a mouse line that allows Cre-mediated inactivation of Numb in RGCs.

To study the role of Numb on neuronal survival, we first analyzed retinal sections from 5- and 20-month-old cDKO compared to Numb$^{+/-}$;Nbl KO and Nbl KO controls (fig. S2, A to K). At 5 months, stainings for the RGC marker Brn3b, the amacrine cell marker Pax6, or the bipolar cell marker Chx10 revealed no significant changes in the number of these cell types in cDKO retinas compared to controls (fig. S2, I to K). In 20-month-old mice, however, we observed a threefold reduction in the number of RGCs in cDKOs (fig. S2, L, M, R, S, and V), whereas the number of amacrine and bipolar cells was unchanged (fig. S2, N to Q, T, and U). As *Nbl* is null in all conditions examined, these results indicate that Numb is specifically required for the long-term survival of RGCs but dispensable for bipolar and amacrine cell survival. To reinforce this finding and determine the time course of RGC loss, we prepared retinal flatmounts from 5-, 8-, and 20-months-old mice and counted the number of Brn3b$^+$ RGCs (Fig. 1M). At 5 months, the total number of RGCs was similar in all genotypes examined and not significantly different from WT mice, consistent with our observations in retinal sections (Fig. 1, A to D and M, and fig. S2K). Starting in 8-month-old animals, however, we observed a significant decrease in RGC numbers in cDKO animals (Fig. 1, E to H and M), which progressed to about 50% loss of RGCs at 20 months (Fig. 1, I to L and M). The number of RGCs in Nbl KO mice was not different from that of WT animals at any age examined, indicating that Nbl inactivation alone has no effect on RGC survival (Fig. 1M). Although a previous study reported that RGC are normally lost with age in WT mice (*39*), a more recent paper reported no difference in RGC numbers with age (*40*), which is consistent with our data. The reason for these different findings remains unclear. Together, these results show that Numb is required to support the long-term survival of RGCs.

Numb is required to maintain axonal integrity

In many neurodegenerative diseases, damage occurs in axons and dendrites before any cell death is detected (*41*, *42*). To test whether this is the case in cDKO retinas, we evaluated the morphology of intraretinal RGC axons in 5-month-old animals, before any detectable cell loss (Fig. 1M). First, we used DiI to retrogradely label RGC axons in Nbl KO and cDKO mice. While axons of Nbl KO animals appeared smooth and healthy, those from cDKO mice showed extensive blebbing (Fig. 2, A to D), an early sign of neurodegeneration. Second, we used adeno-associated viral vector type 2–expressing green fluorescent protein (AAV2-GFP), which preferentially infects RGCs after intravitreal injection (*43*), to label RGC axons in Nbl KO or cDKO animals. As observed with DiI, axonal blebbing was extensive in cDKO RGCs but not in Nbl KO (Fig. 2, E and F). Because intraretinal axons are nonmyelinated, we next wondered whether myelinated RGC axons in the optic nerve also display blebbing. To address this question, we generated transverse sections of optic nerves and imaged GFP after AAV2-GFP intraocular injection and the tdT reporter (Fig. 2, G to N). With both markers, we observed axonal blebbing in the optic nerve of cDKO mice but not in Nbl KO or Numb$^{+/-}$; Nbl KO mice, as observed in nonmyelinated intraretinal axons. We next asked whether these axonal defects were cell autonomous. To do this, we cultured primary RGCs from postnatal day 8 (P8) Numb$^{+/-}$; Nbl KO and cDKO mice and counted the number of axonal blebs 14 days later using the tdT reporter and immunostaining for neurofilament 165-kDa subunit (NF165), a marker of RGC axons. As observed in vivo, RGCs from cDKO mice had significantly more blebs compared to Numb$^{+/-}$; Nbl KO, whereas total neurite length and number of branches were not affected (Fig. 2, O to V). We also observed that loss of Numb and Nbl leads to dendritic fragmentation in RGCs in vivo at young ages (fig. S3), as observed in the retina of aged WT mice (*40*), suggesting that loss of Numb/Nbl accelerates aging in RGCs. Together, these results indicate that axonal blebbing occurs before RGC degeneration in cDKO mice and that Numb functions cell autonomously to maintain neurite integrity in RGCs.

Numb negatively controls intraneuronal tau levels

In tauopathies, the accumulation of Tau proteins is often associated with the formation of axonal blebs (*44*, *45*), as we observed in cDKO RGCs. Consistently, we found that the axonal blebs observed in cDKO RGCs are filled with Tau (Fig. 2Y). We therefore hypothesized that cDKO RGCs might have abnormal levels of Tau. To test this idea,

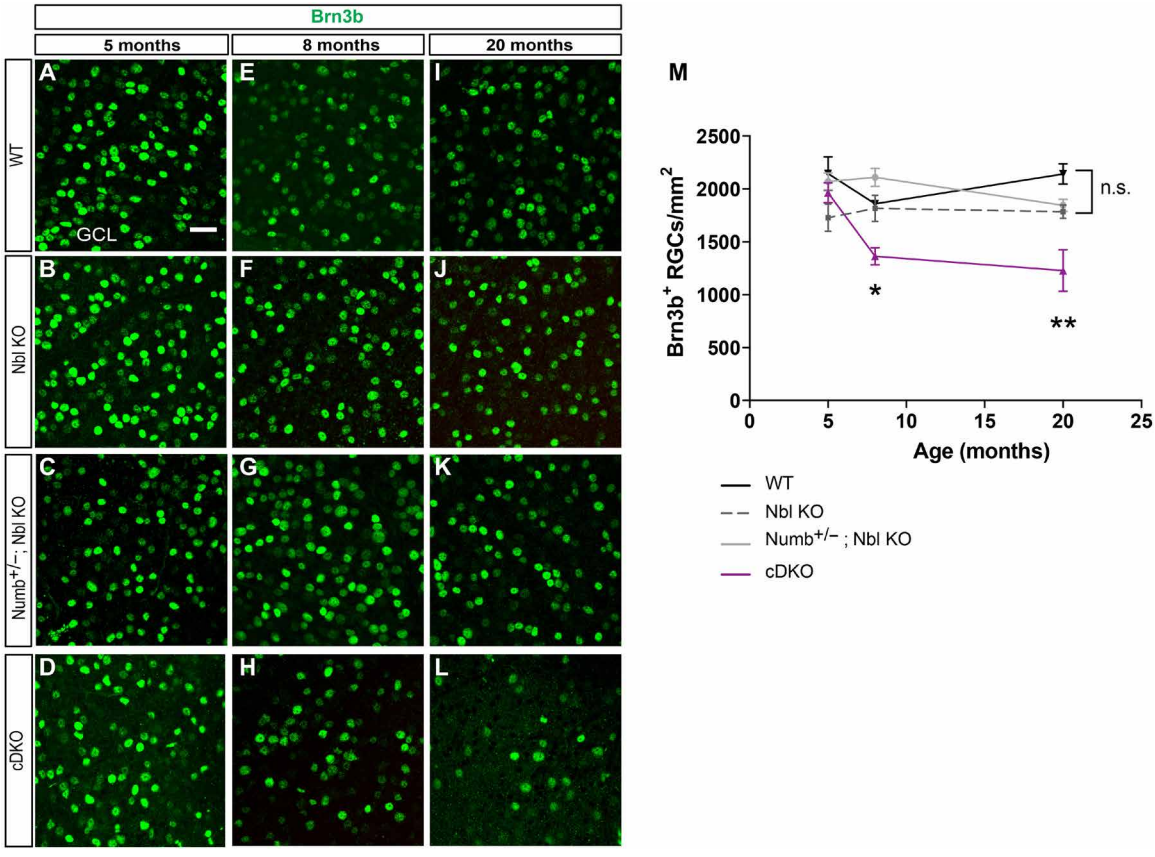

Fig. 1. Numb is essential for long-term survival of RGCs. (**A** to **L**) Single-plane confocal images of retinal flat mounts stained for Brn3b from 5- (A to D), 8- (E to H), and 20-month-old (I to L) WT, Nbl KO, Numb$^{+/-}$; Nbl KO, and cDKO mice, as indicated. Images were taken in the ganglion cell layer (GCL). Scale bar, 30 μm. (**M**) Quantification of the number of Brn3b^{+} RGC per mm^{2} in WT, controls, and cDKO mice at 5, 8, and 20 months old. Means ± SEM, $n = 5$ animals per genotype per time point. *$P \leq 0.05$ and **$P \leq 0.01$, two-way ANOVA followed by Turkey's test. n.s., not significant.

we prepared optic nerve protein extracts from 5-month-old cDKO animals and assessed total Tau levels by Western blot using two different antibodies against Tau: the 5A6 antibody, which was raised against human Tau, but we found that it also recognizes mouse Tau (fig. S4A), and the K9JA antibody raised against mouse Tau. With both antibodies, we found that the levels of total Tau in cDKO optic nerves are higher than in Nbl KO optic nerves (Fig. 3, A and B, and fig. S4, B to D), whereas acetylated tubulin was not changed (Fig. 3A), suggesting that the elevation in Tau levels is not a consequence of destabilized microtubules. The levels of toxic oligomers were also sharply increased in cDKO optic nerve extracts, as detected by Western blots using two different antibodies against oligomeric Tau (Fig. 3, C to E, and fig. S4, E and F). Of note, we found no changes in the levels of two different phosphorylated forms of Tau (pTau) in cDKO optic nerves (fig. S4, G to J) compared to Nbl KO, suggesting that elevation of Tau oligomers in cDKO occurs in a phosphorylation-independent manner, although we cannot exclude that other pTau not tested here might be altered in cDKO. Moreover, we found no change in *Tau* mRNA levels in cDKO (fig. S4K), indicating that Numb does not regulate Tau transcription. Together, these results show that Numb is required to negatively regulate total Tau protein levels in RGCs and prevent the accumulation of oligomeric Tau.

On the basis of the above results, we postulated that the increased Tau levels observed in RGC axons might be the cause of neurodegeneration in cDKO retinas. If this were the case, then we predicted that elevating Tau levels in WT RGCs would phenocopy the loss of Numb, whereas knocking down Tau in cDKO RGCs would rescue degeneration. To test these predictions, we first overexpressed GFP-fused WT human Tau (Tau::GFP) or TauP301L (TauP301L::GFP), a mutant form of Tau associated with tauopathies, in cultured WT mouse RGCs and quantified axonal blebs 14 days later. As predicted, overexpression of Tau::GFP or TauP301L::GFP significantly increased axonal blebbing compared to GFP expression alone (Fig. 3, F to I), indicating that the overall levels of Tau are critical to RGC axonal integrity. Next, we wanted to determine whether lowering Tau levels could rescue degeneration of cDKO RGCs in vivo. As shown in Fig. 1, however, significant loss of neurons is not detected before 8 months of age in cDKO mice, rendering this experiment difficult. To circumvent this issue, we sought to accelerate cell death in cDKO animals. To do this, we injected low doses of *N*-methyl-D-aspartate (NMDA) in the eyes of Nbl KO and cDKO mice to induce a mild excitotoxic stress (*46*, *47*). At this dose of NMDA, the number of Brn3b^{+} RGCs was reduced by 50 to 60% in Nbl KO 3 days after injection compared to saline-injected controls (Fig. 3, J to P), whereas the same dose reduced RGC numbers by an additional 50% in

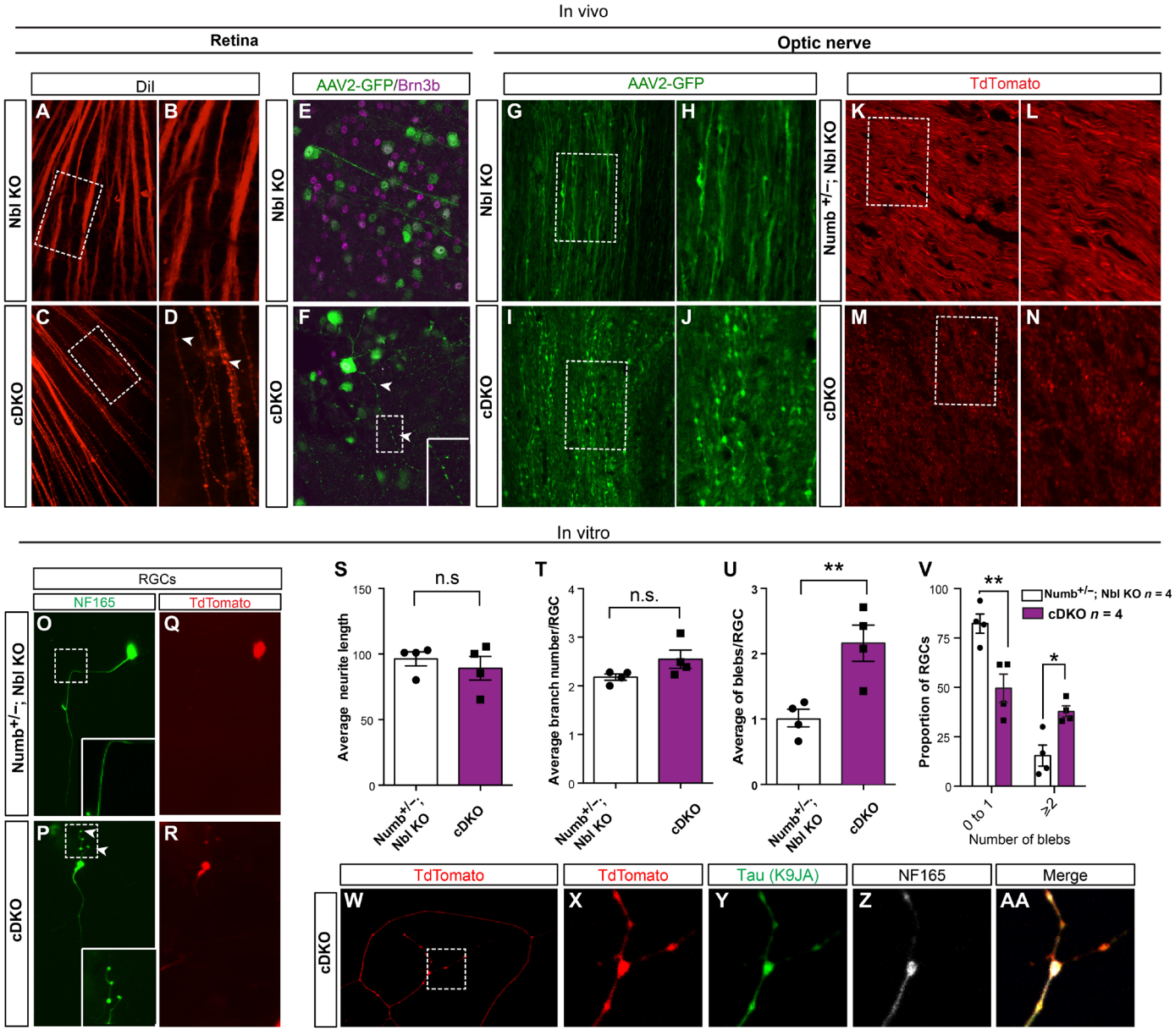

Fig. 2. Numb is essential to maintain axonal homeostasis. (**A** to **D**) Confocal images of DiI-labeled RGC axons in retinal flat mounts from 5-month-old Nbl KO (A and B) and cDKO (C and D). Magnified views of the boxed regions in (A) and (C) are shown in (B) and (D). Arrowheads point to blebbing. (**E** and **F**) Confocal images of AAV2-GFP–infected Nbl KO (E) and cDKO (F) RGCs immunostained for Brn3b on retinal flatmounts. Arrowheads point to axonal blebs. (**G** to **J**) Confocal images of transverse sections of optic nerves from AAV2-GFP–infected Nbl KO (G) and cDKO (I). Magnified views of the boxed regions are shown in (H) and (J). (**K** to **N**) Confocal images of tdT expression in transverse sections of optic nerves from Numb$^{+/-}$; Nbl KO (K) and cDKO (M). Magnified views of the boxed regions are shown in (L) and (N). (**O** to **V**) Primary retinal cell cultures prepared from Numb$^{+/-}$; Nbl KO and cDKO immunostained for NF165 and tdT after 14 days in culture. Insets show magnified views of the boxed area. Arrowheads point to blebbing. (**S** to **V**) Quantification of neurite length (S), branch number (T), and number of axonal blebs (U and V) in Numb$^{+/-}$; Nbl KO and cDKO RGCs. Number of blebs in controls are normalized to 1 in (M). Graphs show means ± SEM, *$P < 0.05$ and **$P \leq 0.001$; Student's t test. A total of 122 neurons in Numb$^{+/-}$; Nbl KO and 155 neurons in cDKO. (V) Graph shows repartition of the number of blebs in different conditions. Two-way ANOVA followed by Turkey's test, means ± SEM, *$P < 0.05$ and **$P \leq 0.001$. A total of 122 neurons were counted in Numb$^{+/-}$; Nbl KO and 155 neurons in cDKO. (**W** to **AA**) Immunostaining for total Tau (K9JA), NF165, and tdT on primary retina cell cultures prepared from cDKO retinas. Magnified view of the boxed region in (W) is shown in (X) to (AA).

cDKO mice (Fig. 3, M and O). As NMDA can also lead to amacrine cell death, we cannot exclude that this might indirectly contribute to RGC death. Nonetheless, these results indicate that cDKO RGCs are more susceptible to stress-induced degeneration than controls, providing a fast and convenient way to study Numb-dependent neurodegeneration. By using this assay, we injected a validated Tau small interfering RNA (siRNA) cocktail (Fig. 3Q) or scrambled siRNA together with NMDA into the vitreous of Nbl KO or cDKO mice

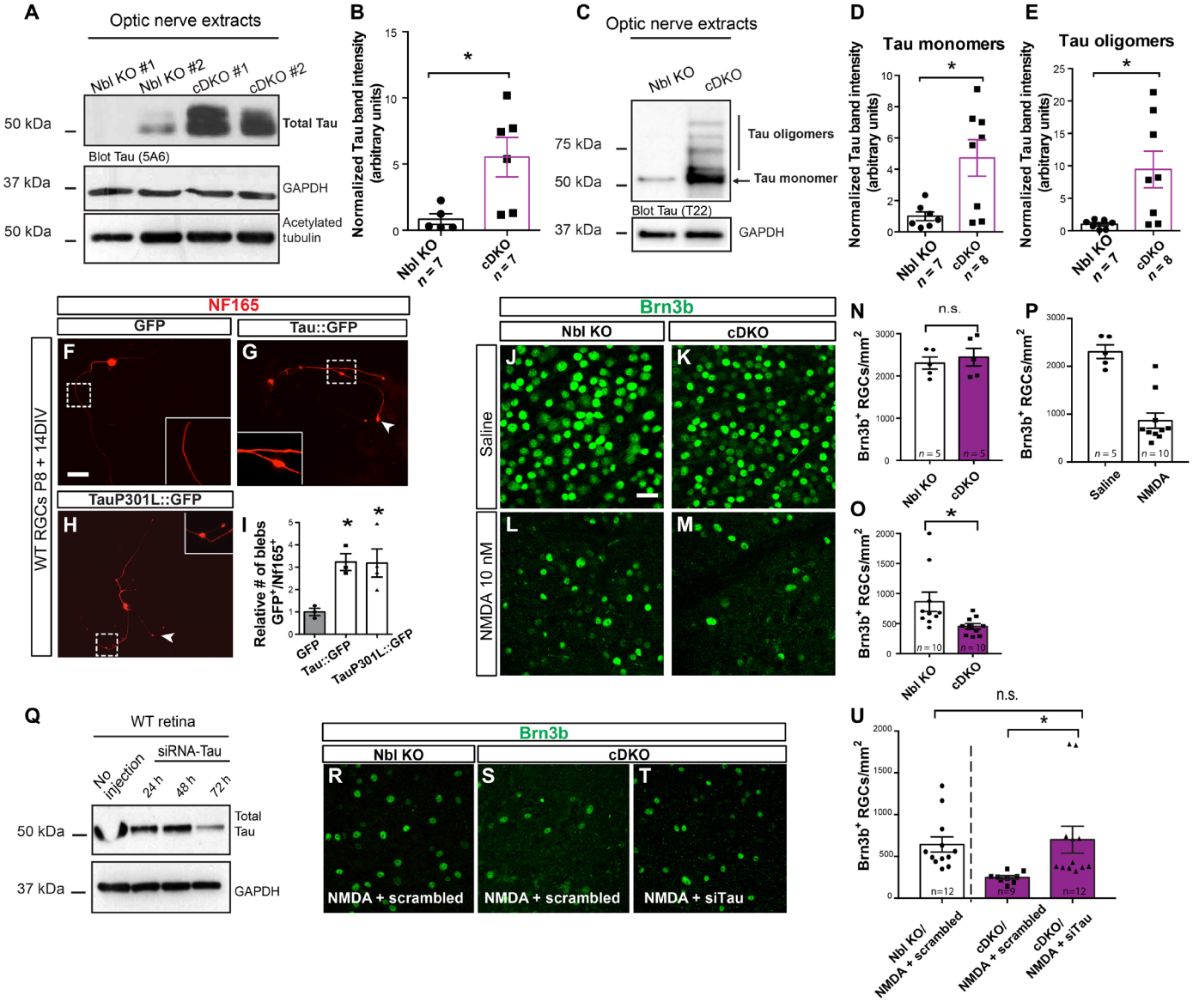

Fig. 3. Tau levels are elevated in Numb cDKO optic nerves and cause RGC death. (**A**) Western blot of total Tau (5A6), GAPDH, and acetylated tubulin expression in optic nerve extracts from 5-month-old Nbl KO and cDKO mice. (**B**) Quantification of Tau level relative to GAPDH. Graph shows means ± SEM, $*P \leq 0.05$; Student's *t* test. (**C**) Western blot (T22 antibody), which recognizes both Tau monomer (50 kDa) and oligomer (>50 kDa), on optic nerve extracts from 5-month-old Nbl KO and cDKO mice. (**D** and **E**) Quantification of Tau monomers (D) and oligomers (E) relative to GAPDH. Graph shows means ± SEM, $*P \leq 0.05$; Student's *t* test. (**F** to **H**) Primary retinal cell cultures 14 days after transfection with GFP (F), Tau::GFP (G), and TauP301L::GFP (H) stained for NF165. Arrowheads point to blebs. (**I**) Number of blebs/RGC. Graph shows means ± SEM, $*P \leq 0.05$; ANOVA one-way test followed by Dunnett's test. $n = 101$ cells for GFP, $n = 92$ for Tau::GFP, and $n = 82$ for TauP301L::GFP. (**J** to **M**) Immunostaining for Brn3b on retinal flatmounts from 5-month-old mice 72 hours after saline (J and K) or NMDA (L and M) injection. Scale bar, 30 μm. (**N** and **O**) Quantification of the number of Brn3b$^+$ RGCs per mm^2 72 hours after saline (N) or NMDA (O) injection. Graph shows means ± SEM, $*P \leq 0.05$; Student's *t* test. (**P**) Number of Brn3b$^+$ RGCs per mm^2 in WT mice 72 hours after saline or NMDA injection. Graph shows means ± SEM. (**Q**) Western blot of total Tau and GAPDH expression in retinal extracts 24, 48, or 72 hours after intravitreal injection of siRNA against Tau. (**R** to **T**) Immunostaining for Brn3b on retinal flat mounts from 5-months-old mice 72 hours after NMDA and scramble siRNA (R and S) or siTAU (T) injection. Scale bar, 30 μm. (**U**) Number of Brn3b RGCs per mm^2 72 hours after NMDA and siRNA injection. Graph shows means ± SEM, $*P \leq 0.05$; ANOVA one-way followed by Turkey's test.

and compared RGC numbers 3 days later. We found that knocking down Tau completely rescues neurodegeneration in cDKO RGCs (Fig. 3, R to U). These results indicate that elevated Tau levels are responsible for neurodegeneration in cDKO mice.

Numb delays Tau-mediated neurodegeneration in a mouse model of tauopathy

The above results indicate that Numb is required to control intracellular levels of Tau and promote neuronal survival. In light of

these findings, we postulated that loss of Numb might exacerbate neuronal degeneration in a model of tauopathy, wherein elevated Tau levels correlate with neuronal cell loss (*48*). To test this hypothesis, we generated a mouse line in which *Numb* and *Nbl* are inactivated on a TauP301S transgenic background (cDKO;TauP301S), a mouse model of tauopathy in which Tau levels in RGCs are five times those observed in control mice (*7*). We then compared RGC numbers at 8 months old in Nbl KO;TauWT, which have the same number of RGCs as WT mice (see Fig. 1M), to that of (i) Nbl KO;TauP301S, (ii) cDKO;TauWT, and (iii) cDKO;TauP301S. While Nbl KO;TauP301S and cDKO;TauWT mice had a similar reduction of RGC numbers, we found that cDKO;TauP301S mice have an even greater reduction of RGCs (Fig. 4, A and B). These results show that Numb functions to slow down RGC degeneration in the context of tauopathy.

We next wondered whether the prosurvival activity of Numb in tauopathies extends beyond RGCs to other neuronal cell types. To address this question, we capitalized on the fact that the Islet1-Cre driver used to generate the cDKO mouse line is also active in developing spinal motoneurons from embryonic day 10.5 (*49*, *50*) and in mature motoneurons of the medial lateral motor column (LMC_M) of the spinal cord (*51*), allowing for inactivation of Numb in these cells. TauP301S mice were also previously reported to exhibit progressive spinal motoneuron degeneration and clasping of the hindlimb, which eventually progresses to complete paralysis and inability to feed (*52*–*55*). This provided an opportunity to test whether loss of Numb would accelerate motoneuron degeneration and the appearance of motor phenotypes in TauP301S mice.

We first sectioned spinal cords in the L3 and L4 lumbar region and counted the number of motoneurons in the LMC_M by staining for choline acetyltransferase (ChAT), a pan-motoneuron marker. In cDKO; TauWT mice, we found similar numbers of motoneurons at 600 days as in WT mice at 350 days (fig. S5, D and G to H), indicating that, unlike in the retina, Numb and Nbl are not essential for long-term survival of motoneurons in the context of WT Tau expression. In TauP301S mice, we found a decrease in the number of $ChAT^+$ motoneurons compared to WT, as previously reported (*53*), although the loss of motoenurons was detected later in our mice at 325 to 350 days. The decrease in motoneurons was significantly more important in cDKO;TauP301S mice at both the L3 and L4 level (Fig. 4, C and D). Consistently, histological analysis of the spinal cord showed a reduction of large soma neurons in the LMC_M of cDKO;TauP301S compared to TauP301S (fig. S5, A to C), indicating that the reduced number of $ChAT^+$ cells reflects motoneuron loss rather than down-regulation of ChAT. These results indicate that Numb/Nbl normally function to delay spinal motoneuron degeneration in the context of tauopathy.

To study motor function, we tested the hindlimb clasping response at different ages as an indicator for the severity of paralysis (*56*, *57*). We defined three stages of clasping depending on the distance observed between the hindlimbs when raising the mouse by the tail (Fig. 4E), as previously described (*58*). We followed mice in the TauP301S and cDKO;TauP301S group over time and observed that stages 2 and 3 are reached on average significantly earlier in cDKO; TauP301S mice (Fig. 4, F and G), and 100% of cDKO; TauP301S animals displayed a stage 3 clasping response by 390 days, whereas it took 501 days to reach this stage in 100% of TauP301S mice (Fig. 4H). Of note, we found no difference in the age of paralysis between females and males (fig. S5, E and F). The cDKO;TauP301S animals also presented a hunched spine in the hindlimb region (Fig. 4H) and failed to grab the cage in an upside-down position at a younger age than TauP301S mice (movies S1 and S2), consistent with the precocious development of the clasping phenotype. As predicted, on the basis of our observation that motoneurons do not degenerate in cDKO;TauWT animals (fig. S5, G to I), we observed no paralysis in these animals (Fig. 4H). Together with our observations in the retina, these results indicate that Numb promotes neuronal survival in the context of tauopathy in multiple neuronal cell types.

Numb negatively regulates intracellular Tau levels in an isoform-specific manner

As inactivating Numb results in increased Tau levels and neurodegeneration in both WT and tauopathy mice, we postulated that elevating Numb might conversely reduce Tau levels and promote neuronal survival. Given the known role of Numb as an adaptor protein, we first asked whether it could physically interact with Tau. We found that each of the four isoforms of Numb coimmunoprecipitate with Flag-tagged Tau when expressed in human embryonic kidney (HEK) 293T cells (Fig. 5, A and B), consistent with physical interaction. To determine whether Numb regulates intracellular Tau levels, we first coexpressed each isoform of Numb together with Tau::GFP in HEK293T cells and analyzed the levels of Tau::GFP by Western blot 72 hours after transfection. While Numb-65, Numb-66, and Numb-71 had no effect, Numb-72 reduced the levels of Tau::GFP (Fig. 5, C and D). To provide a more quantitative measurement of this effect, we used a human medulloblastoma–derived cell line (DAOY) expressing DsRed together with Tau::EGFP downstream of an internal ribosomal entry site (IRES) (*12*). This cell line allowed us to test the effects of Numb expression on Tau levels by reading out GFP fluorescence intensity while using DsRed as a stable fluorescence signal for normalization (Fig. 5E). We transfected DAOY cells with constructs expressing Myc-tagged versions of each of the Numb isoforms or Myc alone as a control and analyzed the relative levels of Tau::EGFP and dsRed by flow cytometry 72 hours later. We found that expression of Numb-72 specifically increases the proportion of cells with low levels of Tau::EGFP, whereas expression of Numb-65, Numb-66, and Numb-71 has no effect compared to Myc (Fig. 5, F to K, and fig. S6A). These results indicate that elevating Numb-72 expression is sufficient to reduce intracellular Tau levels.

To explore how Numb-72 regulates intracellular Tau levels, we first tested whether it could promote proteasome- or lysosome-mediated degradation of Tau (*59*). We transfected DAOY cells with constructs expressing Myc-tagged or Numb-72::Myc, blocked the proteasome or lysosome 48 hours after transfection, and measured the levels of Tau::EGFP and dsRed 24 hours later by flow cytometry. We predicted that if Numb-72 promotes Tau::EGFP trafficking to the proteasome or lysosome, then blocking these pathways would abrogate the effect of Numb-72. We observed that expression of Numb-72 decreases the number of cells with high levels of Tau::EGFP, as observed in our previous experiments, but blocking the proteasome or lysosome has no effect on this activity (fig. S6B), arguing against our hypothesis. Another pathway involved in the regulation of Tau levels is autophagy (*60*), and Numb was previously described to regulate this process (*61*). We therefore analyzed the ratio of autophagy markers LC3-I and LC3-II (*62*) in cDKO optic nerve extracts but found no difference compared to Nbl KO controls, both in native (fig. S6, C and E) and stressed conditions after NMDA injection (fig. S6, D and F). Last, we wondered whether Numb might promote the extracellular release of Tau, which is known to help balance intracellular levels in physiological and pathological conditions

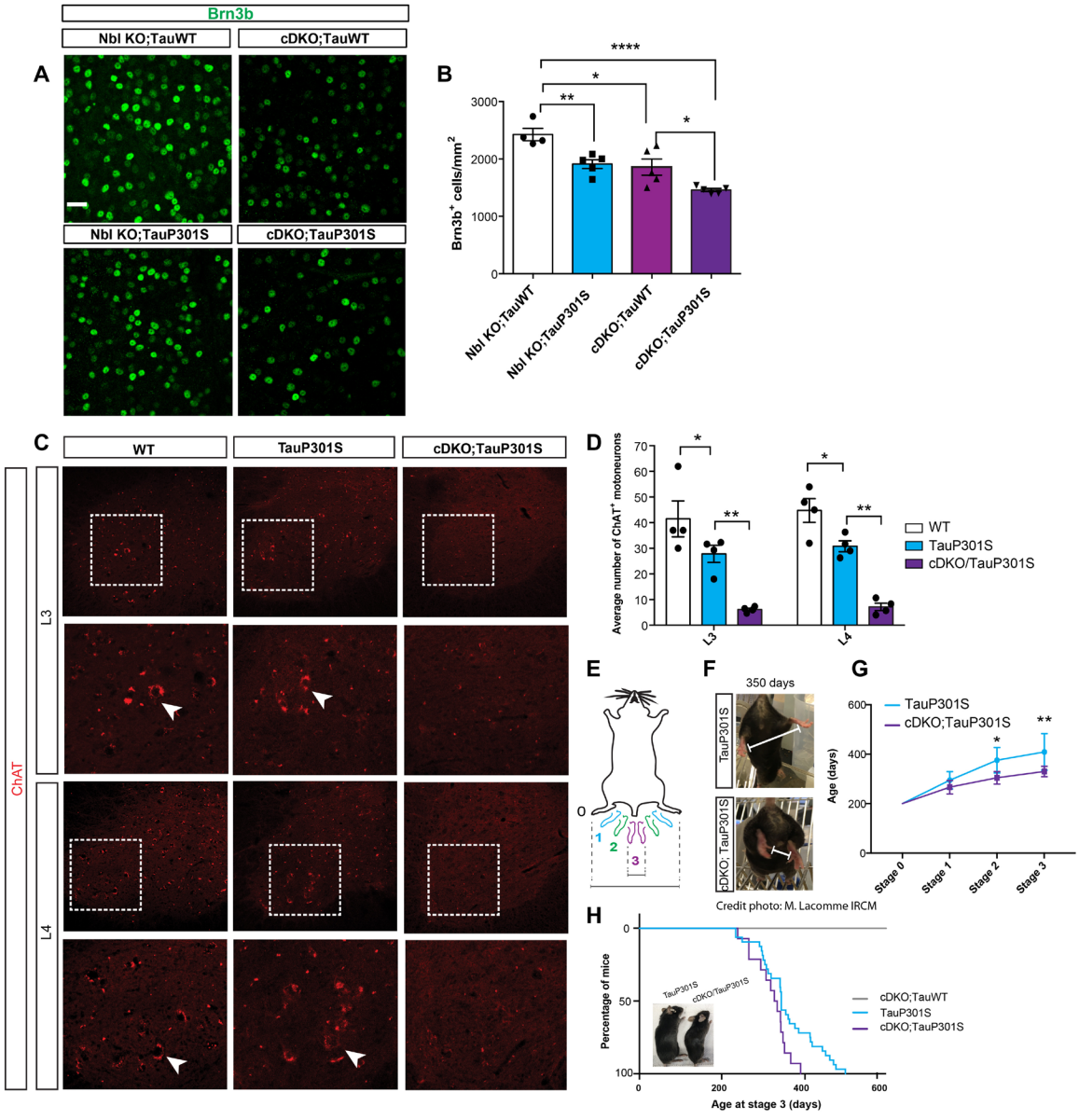

Fig. 4. Loss of Numb in TauP301S mouse accelerates neuronal degeneration. (**A**) Immunostaining for Brn3b on retina flat mounts from 8-month-old Nbl KO;TauWT, Nbl KO;TauP301S, cDKO;TauWT, and cDKO;TauP301S. Scale bar, 30 μm. (**B**) Number of Brn3b$^+$ RGCs per square millimeter in 8-month-old cDKO;TauP301S and the various control genotypes, as indicated. Graph shows means ± SEM, $n = 5$ animals per genotype. One-way ANOVA followed by Turkey's test, $^*P \leq 0.05$, $^{**}P \leq 0.01$, and $^{****}P \leq 0.0001$. (**C**) Immunostaining for choline acetyltransferase (ChAT) on adult spinal cord sections in the lumbar region L3 and L4 of WT, TauP301S, and cDKO;TauP301S mice at 350 days. Arrows point to ChAT$^+$ cells. (**D**) Average number of ChAT$^+$ motoneurons in L3 and L4 in WT, TauP301S, and cDKO;TauP301S. Graph shows means ± SEM, $n = 4$ animals per genotype. Two-way ANOVA followed by Turkey's test, $^*P \leq 0.05$ and $^{**}P \leq 0.01$. (**E**) Schematic representation of paralysis stages based on the clasping reflex, 0 corresponds to no paralysis and 3 to full paralysis of the hindlimbs. (**F**) Representative image of 350-day-old transgenic TauP301S mouse (stage 0) and cDKO;TauP301S mouse (stage 3). (**G**) Comparison of paralysis stages over time in TauP301S ($n = 4$) and cDKO;TauP301S ($n = 5$) mice. Two-way ANOVA followed by Sidak's test, $^*P \leq 0.05$ and $^{**}P \leq 0.01$. (**H**) Percentage of mice at stage 3 over time in cDKO;Tau WT ($n = 6$), TauP301S mice ($n = 32$), and cDKO;TauP301S ($n = 14$). Mantel-Cox test, $^{****}P \leq 0.0001$. Inset shows representative image of hunched spine in the hindlimb region of cDKO; TauP301S at 350 days compared to aged-matched TauP301S.

(*63*, *64*). We transfected GFP or Numb-72 in a Tau-expressing stable cell line and measured the levels of total Tau and oligomeric Tau in the culture medium 24 hours later by dot blot assays. We found that expression of Numb-72 leads to an increase in total Tau levels in the medium (Fig. 5L) but has no effect on the levels of oligomeric Tau released in the medium (Fig. 5M and fig. S6G), at least in this cell line assay.

To determine whether Numb-72 can also promote extracellular release of Tau in neurons, we cultured primary RGCs from TauP301S mice, which have higher levels of intracellular Tau compared to WT RGCs (*30*), and infected them with either AAV2 or AAV2-Numb-72. Four days after infection, we confirmed overexpression of Numb by immunostaining (fig. S6H) and measured the levels Tau released in the medium by dot blot. We observed that Numb-72 leads to increased

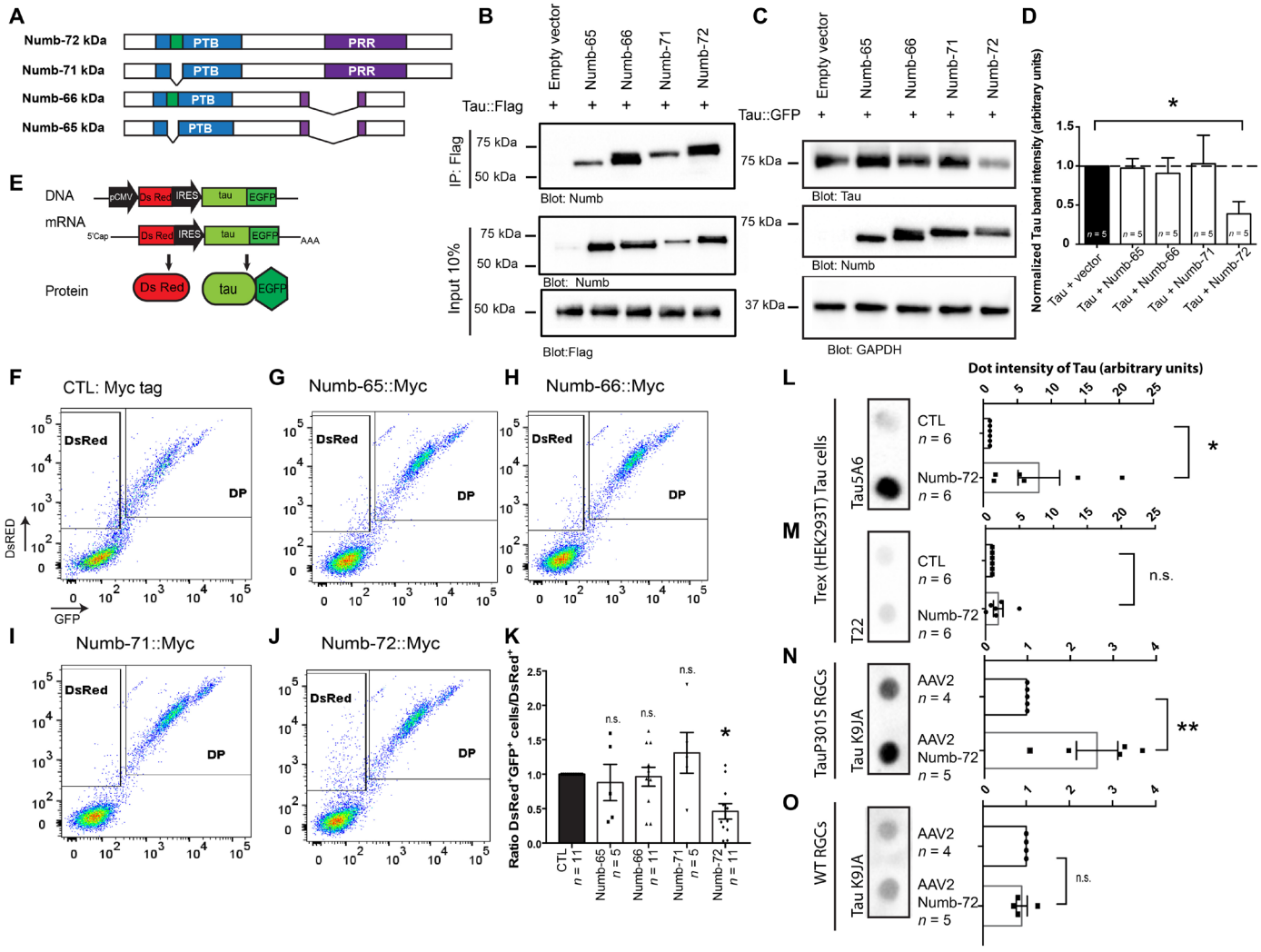

Fig. 5. Numb-72 negatively regulates intracellular Tau levels. (**A**) Schematic representation of Numb isoforms. (**B**) Coimmunoprecipitation (IP) of flag-tagged Tau (Tau::Flag) with each isoform of Numb after coexpression in HEK293 cells. Ten percent input from protein extracts immunoblotted (IB) for Numb or Flag is shown as controls. (**C**) Western blot of Tau::GFP and Numb levels in HEK293 cells 72 hours after coexpression with Numb isoforms. GAPDH is used as loading control. (**D**) Quantification of Tau::GFP levels relative to GAPDH. Graph shows means ± SEM, $*P \leq 0.05$; Student's *t* test. (**E**) Representation of the DNA insertion in the stable human medulloblastoma–derived cell line (DAOY) and resulting mRNA and protein (*12*). (**F** to **J**) Flow cytometry analysis of DsRed and GFP signal in DAOY cells 72 hours after transfection with constructs expressing individual Numb isoforms or the Myc tag alone (CTL). Box area indicates gating used to identify $DsRed^{+}/GFP^{-}$ population. DP, double-positive ($DsRed^{+}/GFP^{+}$) cells. (**K**) Average ratio of $DsRed^{+}/GFP^{+}$ cells over $DsRed^{+}$ cells after expression of the Myc tag control (CTL) and the Numb isoforms. Myc tag value was normalized to 1 and used for comparison with other conditions. Graph shows means ± SEM, $*P \leq 0.05$. One-way ANOVA with Dunett's test. (**L** and **M**) Dot blot analysis of total Tau (Tau5A6; L) and oligomeric Tau (T22; M) detected in culture medium of Tau-expressing HEK293T stable cell line 24 hours after transfection with GFP (Control) or Numb-72-IRES-GFP (Numb-72). Graphs show dot intensity quantification of total Tau or oligomeric Tau signal. Bars show means ± SEM; $*P < 0.05$, Student's *t* test. (**N** and **O**) Dot blot analysis of total Tau (K9JA) levels in culture medium of TauP301S (N) or WT (O) RGCs 4 days after infection with AAV2 or AAV2-Numb-72. Graphs show dot intensity of total Tau signal. Bars show means ± SEM; $**P < 0.001$. Student's *t* test.

Tau release in the medium from TauP301S RGCs (Fig. 5N) but not from WT RGCs (Fig. 5O). These results suggest that Numb-72 promotes the extracellular release of Tau in diseased neurons, which likely contributes to the observed reduction of intracellular Tau levels.

Numb-72 prevents neurodegeneration in mouse models of tauopathy

The identification of Numb-72 as a negative regulator of intracellular Tau levels suggested that it might function as a neuroprotective factor in tauopathies. To test this idea, we first cultured primary RGCs from TauP301S transgenic mice and from the triple transgenic mouse model of Alzheimer's disease (3xTg), which expresses the human mutant version of TauP301L, in addition to the Swedish amyloid precursor protein (APP) mutant, and M146V Presenilin. RGCs were electroporated with constructs expressing GFP alone or Numb-72-IRES-GFP, cultured for 2 weeks, and stained for NF165 to identify RGCs. While neurite length and number of branches were not changed in any condition (Fig. 6, F, G, M, and N), we observed a significant increase in the number of blebs in GFP-transfected TauP301S or 3xTg neurons (Fig. 6, A to E and H to L), consistent with the idea that blebbing is an early sign of neurodegeneration in tauopathies. In contrast, the number of blebs in TauP301S and 3xTg

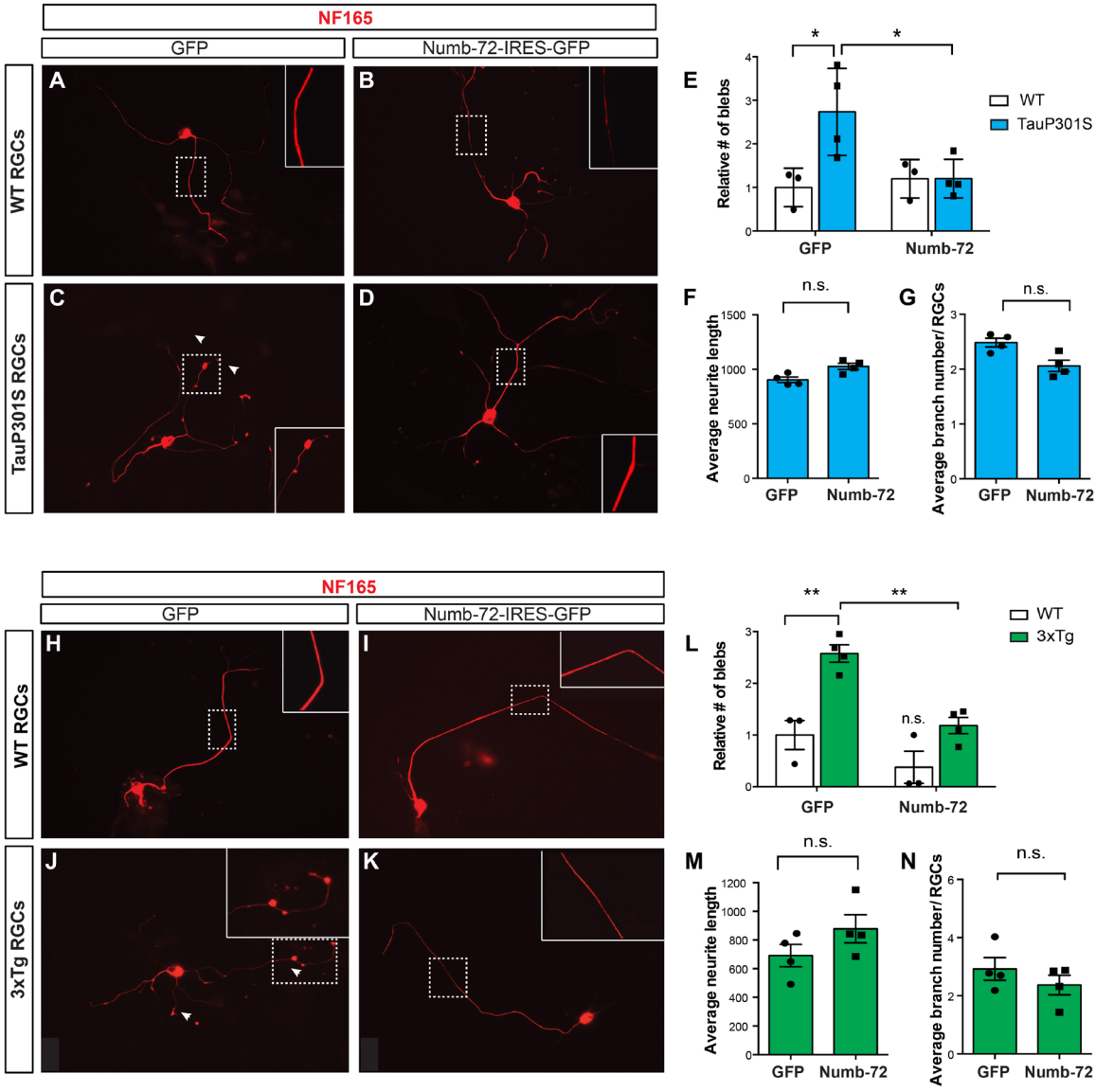

Fig. 6. Numb-72 reduces blebbing in primary RGCs of tauopathy mouse models. (**A** to **D**) Immunostaining for NF165 on primary retinal cell cultures from WT and TauP301S mice 14 days after transfection with GFP or Numb-72-IRES-GFP. An increase in the number of blebs (arrowheads) is observed in TauP301S neurons compared to WT but reversed by Numb-72 expression. Dotted boxes identify regions magnified in insets. (**E** to **G**) Quantification of the number of axonal blebs (E), neurite length (F), and branch number (G) in WT and TauP301S RGCs. Values in WT were normalized to 1. Bar graphs show means ± SEM, $^{**}P \leq 0.001$. Two-way ANOVA followed by Sidak's test (bleb counts) and Student's *t* test (neurite length and branch numbers). $n = 3$ independent cultures for WT (133 GFP-transfected cells and 125 Numb-72–transfected cells analyzed) and $n = 4$ independent cultures for TauP301S (194 GFP-transfected and 121 Numb-72–transfected cells analyzed). (**H** to **K**) Immunostaining for NF165 on primary retinal cell cultures from WT and 3xTg mice 14 days after transfection with GFP or Numb-72-IRES-GFP. An increase in the number of blebs (arrowheads) is observed in 3xTg neurons compared to WT but reversed by Numb-72 expression. Dotted boxes identify regions magnified in insets. (**L** to **N**) Quantification of the number of axonal blebs (L), neurite length (M), and branch number (N) in WT and 3xTg RGCs. Values in WT were normalized to 1. Bar graphs show means ± SEM, $^{**}P \leq 0.001$. Two-way ANOVA followed by Sidak's test (bleb counts) and Student's *t* test (neurite length and branch numbers). $n = 3$ independent cultures for WT (128 GFP-transfected cells and 137 Numb-72–transfected cells analyzed) and $n = 4$ independent cultures for 3xTg (151 GFP-transfected and 119 Numb-72–transfected cells analyzed).

neurons transfected with Numb-72 was not different from that of WT RGCs transfected with GFP (Fig. 6, E and L), indicating that expression of Numb-72 prevents the appearance of neurodegenerative features in cultured neurons from two different mouse models of tauopathy.

Then, we asked whether elevating Numb-72 levels in tauopathy neurons could prevent neurodegeneration in vivo. To deliver Numb-72 RGCs, we generated AAV2 vectors expressing Numb-72 or GFP as control. As previously reported with AAV2, intravitreal injections preferentially infected RGCs (*43*) (Fig. 7, A to C), and the Numb-72–infected RGCs expressed Numb at levels well above baseline (Fig. 7, D to F), validating this vector as an appropriate tool to elevate Numb-72 levels in RGCs in vivo. We injected AAV2-GFP or AAV2-Numb-72 in the vitreous of 5-month-old WT, TauP301S, and 3xTg mice. Seven weeks later, we induced a mild stress by intravitreal injection of NMDA in all mice (as in Fig. 3) and analyzed the number of RGCs 3 days later. In AAV2-GFP–infected retinas, we found that the number of

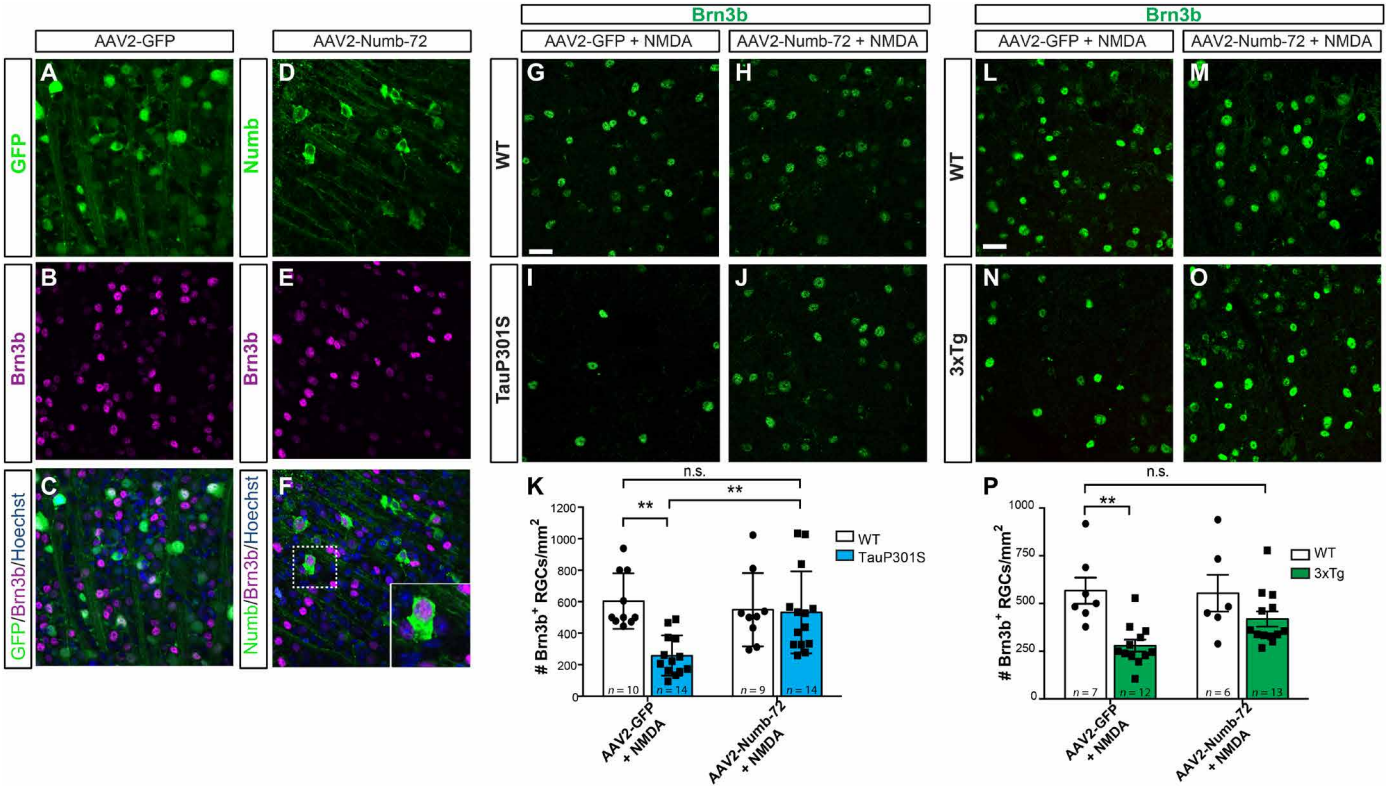

Fig. 7. Numb-72 rescues RGC death in tauopathy mouse models in vivo. (**A** to **C**) Immunostaining for GFP (A) and Brn3b (B) on retinal flatmounts from WT mice, 7 weeks after intravitreal injections of AAV2-GFP in 5-month-old animals. Merged image with Hoechst nuclear stain is shown in (C). (**D** to **F**) Immunostaining for Numb (D) and Brn3b (E) on retinal flatmounts from WT mice, 7 weeks after intravitreal injections of AAV2-Numb-72 in 5-month-old animals. Merged image with Hoechst nuclear stain is shown in (F). Inset shows high magnification view of a Numb/Brn3b double-positive cell. (**G** to **J**) Immunostaining for Brn3b on retina flatmounts from WT (G to H) and TauP301S mice (I to J), 7 weeks after intravitreal injections of AAV2-GFP or AAV2-Numb-72 in 5-month-old animals. Three days before sacrifice, all animals received an intravitreal injection of 10 mM NMDA. Confocal images were taken in the ganglion cell layer. Scale bar, 30 μm. (**K**) Number of Brn3b$^+$ RGC per square millimeter in WT and TauP301S mice after AAV2-GFP + NMDA or AAV2-Numb-72 + NMDA injection. Bar graphs show means ± SEM, $^{**}P \leq 0.001$; two-way ANOVA followed by Turkey's test. (**L** to **O**) Immunostaining for Brn3b on retina flatmounts from WT (L and M) and 3xTg-AD (N and O) mice, 7 weeks after intravitreal injections of AAV2-GFP or AAV2-Numb-72 in 5-month-old animals. Three days before sacrifice, all animals received an intravitreal injection of 10 mM NMDA. Confocal images were taken in the ganglion cell layer. Scale bar, 30 μm. (**P**) Number of Brn3b$^+$ RGC per square millimeter in WT and 3xTg-AD after AAV2-GFP + NMDA or AAV2-Numb-72 + NMDA injection. Bar graphs show means ± SEM, $^{**}P \leq 0.001$; two-way ANOVA followed by Turkey's test.

RGCs is reduced by about 50% in TauP301S and 3xTg mice compared to WT (Fig. 7, G, I, K, L, N, and P), indicating that RGCs in these mouse models are more susceptible to stress-induced cell death, as previously demonstrated (*29*, *31*, *65*). In WT retinas infected with AAV2-Numb-72 or AAV2-GFP, the number of RGCs was comparable, indicating that expression of Numb-72 does not prevent NMDA-mediated neuronal degeneration nor affect survival in WT neurons (Fig. 7, G, H, K, L, M, and P). Notably, however, there was no significant loss of RGCs in TauP301S or 3xTg mice infected with AAV2-Numb-72 compared to WT mice (Fig. 7, H, J, K, M, O, and P). These results indicate that viral vector–mediated delivery of Numb-72 prevents neuronal cell loss in two different mouse models of tauopathy in vivo.

Next, we sought to determine whether the tauopathy neurons protected by AAV2-Numb-72 treatment are functional. To this end, we carried out fluorometric calcium imaging to monitor neuronal activity in cultured RGCs. Of note, intracellular calcium regulation is altered in neurodegenerative diseases, including the TauP301S mouse model (*66*). Thus, we isolated primary RGCs from WT and TauP301S mice and, 1 week later, infected them with either AAV2 or AAV2-Numb-72. Two weeks after infection, we measured intracellular dynamic changes in calcium using Oregon Green 488 AM BAPTA-1 (OGB-1) by time-lapse microscopy. After depolarization with KCl, we observed that TauP301S cells have abnormal calcium spike responses compared to WT, as previously observed in vivo (Fig. 8, A to C and G to I) (*66*). In contrast, TauP301S RGCs infected with AAV2-Numb-72 exhibited a calcium response that was indistinguishable from that of WT RGCs (Fig. 8, D to F and J to L). Moreover, fewer TauP301S neurons displayed calcium spikes in control AAV2-infected cultures compared to WT, as expected, but the proportion of TauP301S RGCs firing after infection with AAV2-Numb-72 was similar to WT RGC cultures (Fig. 8M). These data show that Numb-72 treatment not only prevents neuronal cell death but also improves electrical response in tauopathy neurons.

Last, we asked whether expression of Numb-72 in TauP301S RGCs in vivo could improve visual function. It is well known that binocular vision is largely dependent on RGC function, and loss of RGCs leads to problems in depth perception (*67*). The visual cliff test is classically used to detect these defects (*68*). The test relies on the animals using their binocular vision to detect and avoid the

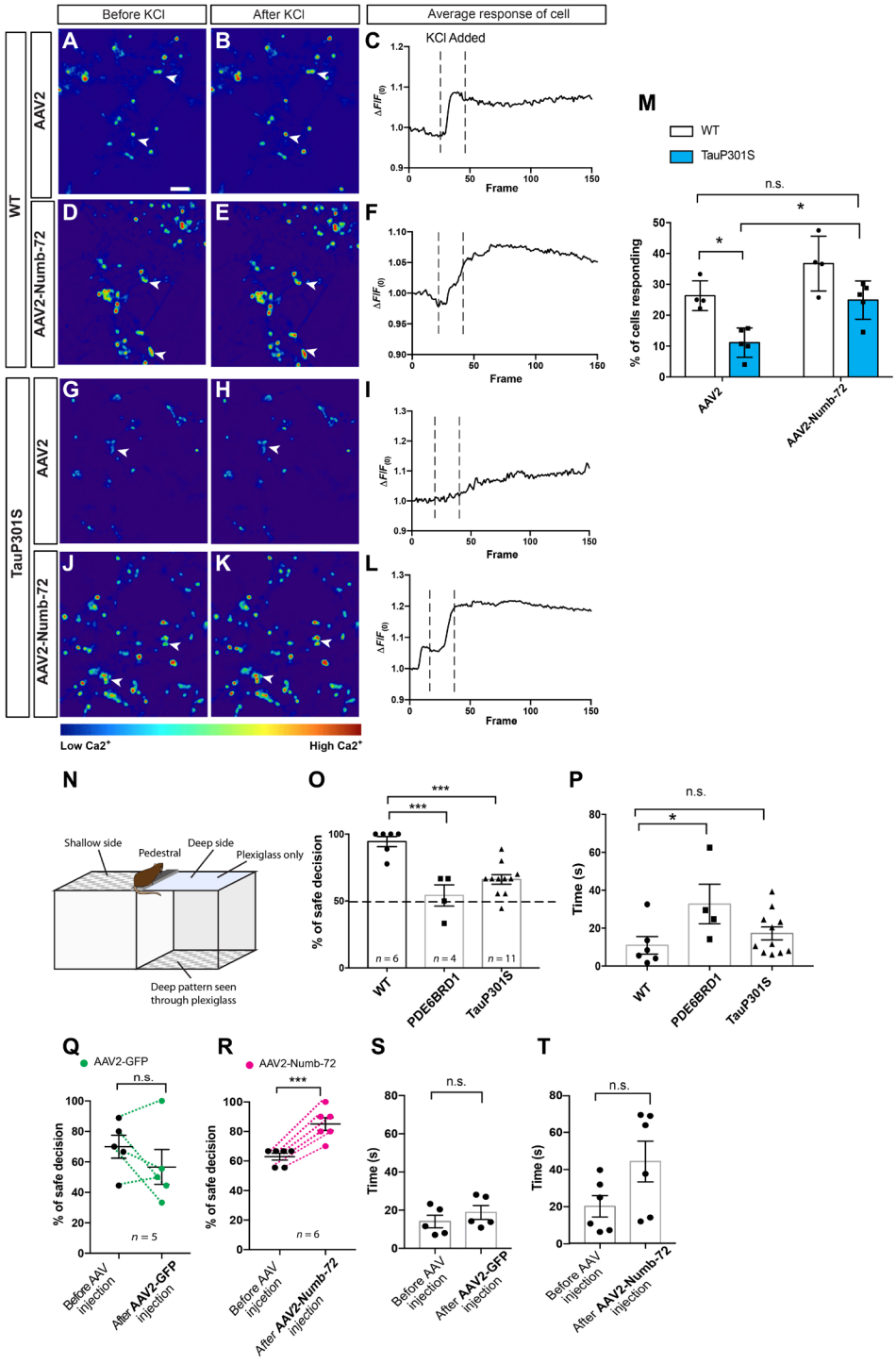

Fig. 8. Numb-72 rescues RGC function in tauopathy mouse models in vitro and in vivo. (**A**, **B**, **D**, **E**, **G**, **H**, **J**, and **K**) Pseudo-colored images of calcium (Ca^{2+}) activity before (A, D, G, and J) and after (B, E, H, and K) addition of KCl. (**C**, **F**, **I**, and **L**) Traces representing the average change of Ca^{2+} sensor fluorescence relative to baseline ($\Delta F/F_0$). A minimum of 70 cells per condition were analyzed, $n = 4$ independent experiments per group. (**M**) Percentage of cells in culture that showed a Ca^{2+} spike in WT and TauP301S RGC culture infected with AAV2 or AAV2-Numb-72. Bar graphs show means ± SEM, $^*P \leq 0.05$; two-way ANOVA followed by Turkey's test. $n = 4$ WT individual cultures; $n = 5$ TauP301S individual cultures (minimum of 95 regions of interests analyzed). (**N**) Schematic of the cliff test apparatus. Mice are placed in the pedestal and chosen between a deep side and a safe shallow side. (**O**) Histogram represents the percentage of safe decisions. Bar graphs show means ± SEM, $^{***}P \leq 0.0001$ and $^{**}P \leq 0.001$; one-way ANOVA followed by Turkey's test. $n = 6$ WT, $n = 4$ PDE6BRD1, and $n = 11$ TauP301S. (**P**) Average of time to make a decision. Bar graphs show means ± SEM, $^*P \leq 0.05$; one-way ANOVA followed by Turkey's test. (**Q** and **R**) Percentage of safe decisions before AAV injection [same animals as in (O)] and 7 weeks after AAV2-GFP (Q) or AAV2-Numb-72 (R). Bar graphs show means ± SEM, $^{**}P \leq 0.001$. Paired *T* test. (**S** and **T**) Average time that TauP301S mice spend to decide before [same animals as in (P)] and after AAV2-GFP (S) or AAV2-Numb-72 (T). Bar graphs show means ± SEM, paired *T* test.

deep side of the box, instead favoring the shallow side (Fig. 8N). We first tested WT mice, PDE6B RD1 mice, which are blind due to photoreceptor degeneration, and TauP301S mice around 120 days (before any paralysis). As expected, WT mice preferred the shallow side of the box almost 100% of the time, whereas PDE6B RD1 mice equally selected either side, reflecting their inability to see (Fig. 8O). Similarly, TauP301S animals have significantly less preference for the "safe" shallow side compared to WT (Fig. 8O), consistent with previous reports showing reduced RGC response of in these mice (*69*). Decision time was the same for TauP301S and WT mice and slightly increased in PDE6E RD1 mice (Fig. 8P). After this first round of testing, the TauP301S mice received a binocular intravitreal injection of AAV2-Numb-72 or AAV2-GFP and were retested on the visual cliff 7 weeks later. We found that three of five mice that received an AAV2-GFP injection now selected the deep or shallow side randomly (Fig. 8Q), indicating a worsening of their binocular vision, whereas all six mice that received binocular injections of AAV2-Numb-72 improved their performance in the visual cliff test compared to before the injections (Fig. 8R). All mice showed no change in decision time (Fig. 8, S and T). These results show that Numb-72 expression in tauopathy RGCs improves visual function in vivo.

DISCUSSION

Our findings indicate that Numb negatively regulates intracellular Tau levels, thereby preventing toxic accumulation of Tau oligomers and neurodegeneration. We also demonstrate that neuronal expression of the long isoform of Numb in two different mouse models of tauopathy prevents neurodegeneration and improves neuronal function, opening the door to the development of unprecedented therapeutic approaches for tauopathies.

The role of Numb and Nbl has been extensively studied in the developing nervous system, where they control neural progenitor cell fate decisions in the neocortex (*36*, *70*), retina (*32*, *33*, *71*, *72*), and spinal cord (*19*). In contrast, their role in mature neurons is not as well established. While Numb/Nbl inactivation disrupts axonal arborization in sensory neurons (*19*), axonal growth of hippocampal neurons (*20*), and guidance of commissural neurons in the neural tube (*21*), these studies did not report an increase of neuronal cell death, which is in contrast with the present study. Previous studies did not evaluate neuronal cell loss in aged animals, whereas our data indicate that significant neuronal cell loss is not detected in the retina before 8 months in Numb/Nbl cDKO. Similarly, we previously reported that inactivation of Numb/Nbl in mouse rod photoreceptors leads to late-onset degeneration (*32*). In spinal motoneurons, however, we find here that inactivation of both Numb and Nbl has no effect on survival, even in 2-year-old animals, suggesting cell-specific functions under normal physiological conditions. In pathological contexts such as in the TauP301S mice, inactivation of Numb/Nbl accelerates degeneration of both motoneurons and RGCs, suggesting a crucial prosurvival role when Tau levels are pathologically elevated. Loss of Numb/Nbl also accelerates the time of onset of motor deficits observed in TauP301S mice, consistent with the observed motoneuron loss. As the late onset of neurological phenotypes is often cited as a limitation for using TauP301S mice as disease models, our findings suggest that Numb/Nbl cDKO; TauP301S mice might represent a more convenient model for some studies.

Our findings indicate that Numb can compensate for the loss of Nbl in RGCs, as Nbl inactivation alone is not sufficient to cause RGC death, even in old mice. Conversely, it remains unknown whether Nbl can compensate for the loss of Numb, as all mouse genetics experiments reported here were carried out in an Nbl KO background for simplicity. In several other contexts, however, mutual functional redundancy between Numb and Nbl was observed (*36*, *73*), including in the retina where Nbl was found to compensate for the loss of Numb in photoreceptor survival (*32*). On the basis of these observations, we speculate that Nbl might also compensate for the loss of Numb in RGCs, but addressing this question definitively will require further investigation.

Before neuronal cell loss, the first sign of degeneration detected in cDKO neurons is axonal blebbing, both in vivo and in culture, as observed in various neurodegeneration models (*41*, *42*). Because inactivation of Numb in RGCs leads to elevation of Tau monomer and oligomer levels, we postulate that this elevation of Tau disrupts axonal transport, which eventually leads to cell death (Fig. 9A), consistent with previous findings showing a role for Tau in axonal transport (*74*, *75*). Our findings that overexpression of Tau in WT RGCs induces blebbing combined with results showing that knocking down Tau in cDKO RGCs rescues NMDA-mediated cell death also support a model in which elevation of Tau in cDKO RGCs is the cause of axonal blebbing and neuronal cell death.

Tau oligomers are the precursors of neurofibrillary tangles and are thought to play a crucial role in the onset and propagation of tauopathies (*6*, *76*, *77*). Our data show that loss of Numb leads to accumulation of both monomeric and oligomeric forms of Tau in the optic nerve, identifying a crucial role for Numb in the regulation of intraneuronal levels of Tau. While elucidating the precise molecular mechanisms by which Numb controls Tau levels will require further investigation, our findings indicate that Numb-72 promotes the release of native Tau monomers into the extracellular space. Several studies have shown that Tau not only is an intraneuronal protein but also can be released in the extracellular space via exosomes and ectosomes (*63*, *64*). Although the release of Tau oligomers was reported to contribute to spreading of the pathology, physiological Tau can also be secreted by neurons through exosomes (*78*, *79*), which is thought to serve as a clearance mechanism to prevent pathological Tau formation (*64*). Consistently, a recent report showed that the transcription factor EB (TFEB), a key regulator of lysosomal biogenesis, is essential for the exocytosis of specific Tau species (*80*). Inactivation of TFEB reduces the levels of Tau in the interstitial fluid in TauP301S mice and increases intracellular Tau levels, translating into enhanced pathology and spreading. By promoting the release of monomeric Tau in the extracellular space, we postulate that Numb-72 expression reduces the pool of Tau available in the cell to form oligomers, contributing to prevent cell death in tauopathies (Fig. 9B). Consistent with this idea, expression of Numb-72 in TauP301S RGCs, which have elevated oligomer levels due to Tau hyperphosphorylation, is sufficient to reduce the number of blebs in culture and fully rescue survival in vivo to the same level as WT RGCs. Expression of Numb-72 also decreases blebbing and neuronal cell loss in the 3xTg Alzheimer's mouse model, albeit to a lesser extent. This observation is not unexpected given that the 3xTg mouse also expresses mutated version of APP and Presenilin. However, since Numb interacts with the cytoplasmic tail of APP, and expression of Numb isoforms containing a PTB insertion (Numb-72 and Numb-66) reduces APP levels in SH-SY5Y cell line (*22*, *81*), these results suggest that Numb-72 expression in 3xTg mice might have dual effect, lowering both Tau and APP levels.

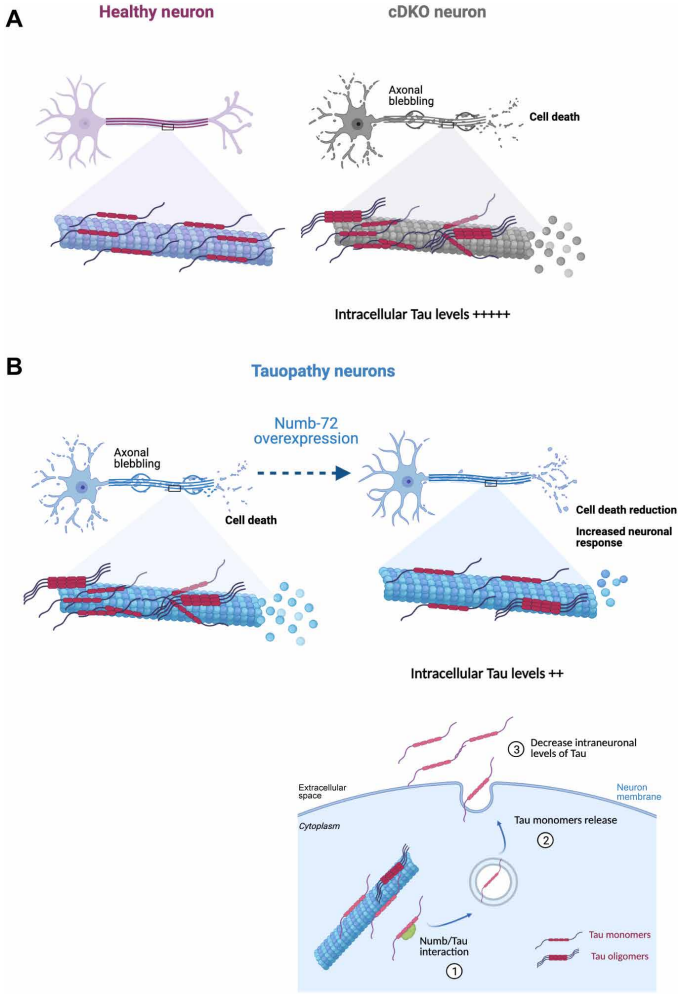

Fig. 9. Model. (**A**) In healthy neurons (left), Numb/Nbl function to maintain Tau homeostasis and promote neuronal survival. In the absence of Numb/Nbl (cDKO, right), intracellular Tau levels rise, leading to formation of Tau oligomers and axonal blebs, followed by cell death. (**B**) In tauopathy neurons, Tau oligomerizes, which leads to axonal blebbing and neurodegeneration (left). Upon expression of Numb-72 in tauopathy neurons, however, the native form of Tau is released in the extracellular space, leading to reduced oligomeric Tau, fewer axonal blebs, and rescued neuronal survival (right). Created with BioRender.com.

As accumulation of Tau is known to disrupt axonal trafficking (*45*), it is plausible that, in addition to promoting survival, lowering intracellular Tau levels would improve vesicle transport in axons and increase neuronal function. Our results are consistent with this idea, as we find that Numb-72 increases electrical response in TauP301S neurons in culture and improves visual performance of TauP301S mutant mice in vivo. Thus, it appears that lowering Tau levels with Numb-72 has multiple beneficial effects, from maintaining survival to promoting neuronal function. While we cannot exclude that expression of Numb-72 in neurons might produce undesirable side effects, we have not observed any signs of toxicity in both WT and mutant neurons. Nonetheless, it will be interesting in the future to carry out structure-function experiments to identify the minimal sequence of Numb-72 required to reduce Tau levels, as this may help generate a synthetic peptide that could be more suitable for clinical translation. Given that the only difference between Numb-72 and the other Numb isoforms lies in sequence insertions in the PRR and PTB domains, it is likely that these regions are involved. Future work will also help determine whether expression of Numb-72 can reduce Tau levels and prevent degeneration of different types of brain neurons, but our findings that inactivation of Numb accelerates neuronal degeneration in both the retina and spinal cord in mouse models of tauopathy suggest widespread prosurvival activity across the CNS.

MATERIALS AND METHODS

Animals

All animal work was carried out in accordance with the Canadian Council on Animal Care guidelines. The Islet1-Cre (*34*), *numb*-floxed (*35*), and *numb-like* null (*37*) mouse lines were used to generate Numb/Nbl cDKO. Female triple transgenic (3xTg) homozygote mice harboring the APPSWE, PS1M146V, and TauP301L transgenes and associated controls (female WT B6J129SF2J) were obtained from the Jackson Laboratory. Transgenic mice (PS19) expressing human TauP301S (1N4R) and the associated controls (WT C57b6J) were obtained from the Jackson Laboratory. We generated cDKO; TauP301S by intercrossing. TauP301S allele is hemizygous in all lines. Transgenic animals are always crossed with nontransgenics to maintain the line. PDE6B mutant mice (RD1) and Mapttm1(EGFP)Klt/TauKO were obtained from the Jackson Laboratory.

Histology and immunohistochemistry

Eyes were enucleated and fixed by immersion in freshly prepared 4% paraformaldehyde (PFA) in phosphate-buffered saline (PBS) solution overnight (O/N) at 4°C, cryoprotected in sucrose 20% (in water) overnight, and cryosectioned at 14 μm. For Numb staining at P0, eyes were fixed in 10% trichloroacetic acid for 10 min and washed with PBS/30 mM glycine before cryoprotection in sucrose 20%. For retina flatmounts, eyes were enucleated after euthanasia and fixed for 2 hours in 4% PFA before PBS wash (3 × 10 min) and dissected to isolate the neural retina, which was flat mounted on microscope slides with RGC facing the coverslip. Sections and flatmounts were preincubated for 1 hour in a blocking solution [1% bovine serum albumin (BSA) in 0.4% Triton] and incubated overnight at 4°C with primary antibodies. Primary antibodies and conditions used in this study are listed in table S1.

Generation of tau stable cell line and cell culture conditions

A stable cell line was generated from Flp-In T-Rex 293 cells (Invitrogen), according to the manufacturer's recommendations. Two micrograms of the POG44 vector that expresses a temperature-sensitive fipase recombinase under the control of the human CMV promoter in combination with 0.5 μg of the vector pCDNA5-FRT/TO-*Tau* was transfected into Flp-In T-Rex 293 cells using the jetPRIME reagent (VRW). Following hygromycin (Thermo Fisher Scientific) selection at 200 μg/ml, a unique clone was selected.

HEK293T and stable cell lines (DAOY and TRex) were cultured in a humidified incubator at 37°C with 5% CO_2 and fed every other day with high-glucose Dulbecco's modified Eagle's medium (DMEM) medium (Thermo Fisher Scientific) supplemented with 10% fetal bovine serum, 2 mM GlutaMAX (Thermo Fisher Scientific), 1 mM sodium pyruvate (Thermo Fisher Scientific), and 1% penicillin-streptomycin (10,000 U/ml; Thermo Fisher Scientific). TRex cells at 50% confluence were treated with tetracycline (1 μg/ml; Millipore-Sigma)

for 24 hours to induce protein expression before transfection for the dot blot assays.

Flow cytometry analysis

The DAOY stable cell line expressing mCherry-IRES-Tau::GFP (*12*) was grown in DMEM medium to 50% confluence and transfected using Lipofectamine 2000 (Thermo Fisher Scientific) with expression constructs encoding Myc, Numb-65::Myc, Numb-66::Myc, Numb-71::Myc, and Numb-72::Myc. To generate these constructs, appropriate complementary DNAs (cDNAs) were cloned into the pCS2 plasmid. Cells were collected after 3 days, dissociated with 0.25% Trypsin-EDTA, and resuspended in PBS. Samples were processed on a BD LSRFortessa (BD biosciences) flow cytometer, and analysis was done using FlowJo software. For protein degradation assays, cells were treated with MG132 (a proteasome inhibitor, 25 μM; Tocris, #1748) or chloroquine diphosphate salt (a lysosome inhibitor, 25 μM; Sigma-Aldrich, #C6628) 48 hours after transfection.

AAV production

AAV vectors were produced as previously described using the cotransfection method and purified by iodixanol gradient ultracentrifugation (*82*). AAV vector stocks were tittered by quantitative PCR (*83*) using SYBR Green (Thermo Fisher Scientific).

Intraocular injections

For DiI (2Z)-2-[(*E*)-3-(3,3-dimethyl-1-octadecylindol-1-ium-2-yl) prop-2-enylidene]-3,3-dimethyl-1-octadecylindole; perchlorate retrograde labeling, eyes were enucleated and fixed overnight in 4% PFA at 4°C. The optic nerve was cut to within a few millimeters of the eye, and a few lipophilic DiI crystals (Invitrogen, D282) were stuffed at the tip of the optic nerve into the optic nerve head. The eyes were then placed into fresh 4% PFA at 37°C for 7 days. Retinas were then dissected, flat mounted in Mowiol, and imaged on an LSM710 (Zeiss) confocal microscope.

Saline, N-methyl-D-aspartate (NMDA) (10 mM Tocris Bioscience], siRNAs (Dharmacon/Horizon), and AAVs were injected in adult eyes according to a modified procedure previously described (*84*). The titers of the AAV serotype 2 used were as follows: 5.5×10^{13} viral genome (vg)/ml for GFP = 1.1×10^{11} vg per retina and 1.63×10^{14} vg/ml = 3.26×10^{11} vg per retina lot1 and 8.3×10^{13} vg/ml = 1.66×10^{11} vg per retina lot 2 for Numb-72. The procedures for construction and purification of AAVs and intraocular injections were described previously (*85*). The volume of the injection was 2 μl. While under isofluorane anesthesia, animals were injected intravitreally with AAV2-Numb-72 in one eye or either vehicle or AAV2-GFP into the contralateral eye as control. The eyes were collected 7 weeks after injections for AAV and after 3 days for the siRNA experiments. All eyes were fixed and processed for immunostaining on flat mount as described above. Scramble siRNA and siTau were generated by Dharmacon/Horizon Discovery group product ON-TARGETplus Smart pool siRNA reagents, and Mouse *Mapt* were resuspended in RNase-free water at 50 μM and used at 10 μM.

RGC cultures

Retinal tissues were dissected from P8 mice, cut in small pieces, and incubated in PBS containing papain (5 mg/ml; Worthington, LS003124), L-cysteine, 0.5 mM EDTA, and deoxyribonuclease I (DNase I; 10 U/ml) for 2 × 3 min. The enzymatic reaction was neutralized in a solution of low-ovomucoid [BSA (Sigma-Aldrich, A-4161) and trypsin inhibitor (Sigma-Aldrich, 10109878001) in PBS] and DNase I (10 U/ml). Tissues were mechanically dissociated by gentle pipetting, and cells were collected as a suspension. Procedures were conducted at room temperature in a laminar flow hood. After centrifugation at 1000 rpm for 11 min, cells were resuspended in RGC medium: Neurobasal (Gibco) supplemented with Sato solution [Apo-transferrin (Sigma-Aldrich, T-1147), BSA (Sigma-Aldrich, A-4161), progesterone (Sigma-Aldrich, P7505), putrescine, sodium selenite (Sigma-Aldrich S5261)], B27 supplement (Invitrogen), penicillin/streptavidin, sodium pyruvate (Gibco), GlutaMAX, *N*-acetyl-cystein (Sigma-Aldrich, A8199), T3 (triiodo-thyronine) (Sigma-Aldrich, T6397), insulin (Sigma-Aldrich, I6634), brain-derived neurotrophic factor (Human Recombinant, PeproTech), and ciliary neurotrophic factor (Rat Recombinant, PeproTech). Cells were then plated on glass coverslips at 50,000 cells per coverslip in a 24-well plate and incubated at 37°C and 8% CO_2 for 2 weeks. Half of the culture medium was changed every 3 days. For RGC transfection, cells were resuspended in Amaxa buffer and supplemented with 2 μg of DNA (Numb-72 was cloned into pCIG-IRES-GFP; GFP was empty vector; and Tau::GFP and Tau::P301L were gifts from N. Leclerc, Université de Montréal) after centrifugation. Then, cells were transferred in an electroporation cuvette, and nucleofection was carried out according to manufacturer's recommendation (Amaxa nucleofector, program #33, Lonza Technology). Glass coverslips were incubated the day before with poly-D-lysine (10 μg/ml) for 1 hour and laminin O/N. For AAV infections, cells were grown for week before infection with 3 μl of virus per well. The viral titers used were as follows: 7.7×10^{12} vg/ml for AAV2-GFP and 8.3×10^{13} vg/ml for AAV2-Numb-72.

Protein extraction, immunoblotting, and immunoprecipitation

For Western blots and immunoprecipitation, HEK293T cells were transfected with the jetPRIME (Polyplus transfection) using the following constructs: Tau::Flag, Tau::GFP (gifts from Dr. N. Leclerc, Université de Montréal), Numb-65, Numb-66, Numb-71, and Numb-72 cloned into a pCIG2-IRES-GFP plasmid.

Cells were harvested and lysed in NP-40 buffer [50 mM tris (pH 8.0), 150 mM NaCl, and 1.0% NP-40 with cOmplete Protease Inhibitor Cocktail from Roche]. For Western blots, 40 μg of protein extract (in vivo) or 10 μg (in vitro) was loaded on 10% acrylamide SDS–polyacrylamide gel electrophoresis gels for separation by electrophoresis and then transferred onto polyvinylidene difluoride membranes using a Trans-Blot (Millipore). The membranes were blocked with 5% milk in tris-buffered saline solution with Tween [TBST; 20 mM tris-HCl, 50 mM NaCl (pH 8.0), and 0.1% Tween]. Immunoblotting with the primary antibody was performed at 4°C overnight in 0.5% dry milk in TBST primary antibodies, and conditions used in this study are listed in table S1. The primary antibody was detected with a horseradish peroxidase (HRP)–conjugated goat anti-rabbit or anti-mouse (1:10,000; Jackson Immunoresearch) in 0.5% dry milk in TBST. HRP activity on the membrane was visualized with the ECL Kit (GE Life Science). For quantifications, we used the Image Lab software (Bio-Rad) to measure band intensity and used glyceraldehyde-3-phosphate dehydrogenase (GAPDH) band intensity for normalization.

For immunoprecipitation, Dynabeads Magnetic Beads (Dynabeads Protein G, Invitrogen) were used according to manufacturer's specifications. Briefly, 40 μl of beads was incubated with primary

antibody for 1 hour at 4°C. One milligram of cell lysate was incubated with the bead-antibody mixture in immunoprecipitation buffer [50 mm tris (pH 8.0), 150 mm NaCl, 5 mm EDTA, and 0.1% NP-40] overnight at 4°C. The beads were separated using a magnet (MagnaBind, Pierce) and washed in Iph buffer. The beads were then boiled in 2× Laemmli buffer at 95°C for 10 min, and the supernatant was used for immunoblotting as described above. We used 10% of cell lysates for input.

For dot blot experiments, we collected culture medium from the Tau-expressing stable cell line 24 hours after GFP or Numb-72 transfection. Culture medium was collected and centrifuged to eliminate cell debris, and then 400 µl of medium was loaded on nitrocellulose membrane. For RGCs (WT and TauP301S), culture medium was collected 4 days after AAV infection and 400 µl was loaded on nitrocellulose membrane and blotted with Tau K9JA antibody (total Tau).

For immunoblotting, the membranes were blocked with 5% milk in TBST and incubated with the primary antibody at 4°C overnight in 0.5% dry milk in TBST (see table S1 for dilution conditions). The primary antibody was detected with an HRP-conjugated goat anti-rabbit or anti-mouse (1:10,000; Jackson ImmunoResearch) in 0.5% dry milk in TBST. HRP activity on the membrane was visualized with the ECL Kit (GE Life Science).

RNA isolation and quantitative PCR

Eyes were dissociated and collected into QIAGEN Buffer RLT plus, and an RNeasy microkit (QIAGEN, 74004) was used to isolate RNA according to the manufacturer's protocol with an additional 2 min of vortex in Buffer RLT. Isolated RNA was reverse-transcribed using SuperScript VILO Master Mix (Thermo Fisher Scientific, 11755050). cDNA was amplified by quantitative PCR using SYBR Green Master mix (Thermo Fisher Scientific, A25742). The primers used for Tau are as follows: forward primer, 5′-CGCCCCTAGTGGATGAGAGA-3′ and reverse primer 5′-GCTTCTTCGGCTGTAATTCCTT-3′. For GAPDH, the primers used are as follows: forward primer, 5′-TGCAGTGGCAAAGTGGAGAT-3′ and reverse primer, 5′-ACTGTGCCGTTGAATTTGCC-3′. All primers were validated using a standard curve dilution of cDNA before the experiments were conducted.

Hindlimb paralysis evaluation

Mice from each group were euthanized as soon as they presented total paralysis. Mice from groups TauP301S and cDKO; TauP301S were followed each day from day 200 onward by lifting the animals by the tail to evaluate hindlimb clasping reflex (stages 1 to 3) to determine the stage of paralysis until they reached full paralysis (stage 3).

Spinal cord sampling and embedding

Mice were anesthetized and transcardially perfused with saline followed by 4% PFA. Spinal cords were removed and cut into cervical, thoracic, lumbar, and sacral segments. For immunohistochemistry, spinal cord tissues were incubated in 20% sucrose in PBS O/N at 4°C, embedded in Optimal cutting temperature compound (OCT)/sucrose (1/1, v/v), then frozen in liquid nitrogen, and stored at −80°C. ChAT immunohistochemistry (see table S1) was carried out on coronal sections of the lumbar spinal cord (16 µm) at the age of 11 months old (325 to 350 days), as described above. Image acquisition and motoneuron number quantification were done on lumbar sections (see the "Quantification" section).

Quantification

RGC survival was assessed by counting $Brn3b^+$ cells on retina flat mounts within four areas of 212 µm by 212 µm around the optic nerve head and averaging the number of cells per square micrometer per retina. Single-plane images were taken with an LSM 710 confocal microscope (Zeiss).

Cell type quantification in retinal sections was done by averaging the total number of positive cells for specific markers in a 250-µm stretch of the central and peripheral retina on four different retinal sections per animal. Images were taken on an LSM710 confocal microscope (Zeiss).

Length of individual isolated RGC neurites was measured on ImageJ by drawing the neurite with the polyline function. Blebs were counted manually. Images were taken with a DM6000 epifluorescence microscope (Leica).

For motoneuron counting, $ChAT^+$ cells located only on the ventral part of spinal cord were counted by applying a fast Fourier transform (FFT) bandpass filter on 16-bit images acquired on a LSM710 confocal microscope (Zeiss) to reduce background. Positive cells were selected by a manually defined fluorescence intensity threshold and automatically counted using the "Analyze Particles" plugin of ImageJ. Minimums of three sections were counted at each level of the lumbar spinal cord that was analyzed per animal. The resulting cell counts were then averaged to give a representative number of the remaining number of motoneurons in that animal.

Dendritic morphology quantification

Using the MATLAB software, we generated a script to identify linear and circular objects. Following image acquisition on a Zeiss LSM710 confocal, a region of interest (the inner plexiform layer) was manually selected for image processing. A threshold intensity value, *th*, was identified from the histogram of the image selection and set as the intensity that represents 15% of the most intense pixels. Objects were than obtained from binary image with an 8-pixel connectivity method. Objects smaller than 2 μm^2 were rejected. Major axis length (from a best fit of ellipse with the object), perimeter (p), and area (A) of objects were measured. To identify elongated objects, we used the ratio, R, where $R = p^2/4\pi A$. Elongated objects were arbitrarily selected as $R > 3.5$ (a ratio of 1 being a perfect disk).

Calcium spike recording

We used primary neurons from P8 TauP301S and WT mice. Neurons were incubated at 37°C in 5 µM Oregon Green 488 BAPTA-1 (AM) for 40 to 45 min and added to a perfusion chamber where they were perfused with AMES medium (Sigma-Aldrich with added sodium bicarbonate) equilibrated with 5% CO_2 at 25°C. Cells were left for 5 min to equilibrate and wash off excess indicator before imaging with a spinning disk microscope (Zeiss). KCl (10 mM) was added at time points indicated. Images were analyzed using the Calima software (*86*). The fluorescence intensity (F) over baseline ($\Delta F/F_0$) was calculated with F_0 (baseline) being $T = 0$. To calculate traces averages, four traces ($n = 4$) were plotted for intensity over time ($\Delta F/F_0$), each graph was made from 70 to 80 cells, and these traces were then combined to make an average for each condition. The rates of change were calculated by taking the time from KCl administration at baseline to highest fluorescence intensity, with each of the four graphs from each condition considered as a single n.

Visually guided behavioral test

A visual cliff test was used to access visual function (see Fig. 8N). A box with a plateform (dimensions of 40 cm by 60 cm) with one half covered with 2.5-cm^2 black checkered paper ("shallow" or safe side) and another half as a 67-cm-deep cliff ("deep side") covered by a transparent plexiglass. The deep side is also covered with 2.5-cm^2 black checker linoleum. The box was placed under light to provide equal illumination. The vibrissae were shaved to eliminate tactile placing responses that could interfere with testing of visual function. Each mouse was subjected to 10 trials. Each trial consisted of placing the mouse on the center platform on the pedestal (a ridge of 1 cm high and 2.5 cm wide) of the visual cliff apparatus and recording the side on which the mouse stepped and the time taken to make the decision. The plexiglass and central pedestal were thoroughly cleaned with Virox after each test. Data are presented as the means ± SEM of 10 independent experiments. We tested only female mice.

Statistical analysis

Data analysis and statistics were performed using Prism 6 by two-way analysis of variance (ANOVA; Sidak), one-way ANOVA followed by a Dunett's or Tukey's post hoc tests, or by a Student's *t* test, as indicated in the legends. For the paralysis assay, we used Mantel-Cox test. All quantifications shown are means ± SEM, unless otherwise indicated. *n* represents the number of biological replicates.

SUPPLEMENTARY MATERIALS

Supplementary material for this article is available at https://science.org/doi/10.1126/sciadv.abm4295

View/request a protocol for this paper from *Bio-protocol*.

REFERENCES AND NOTES

1. L. Qiang, X. Sun, T. O. Austin, H. Muralidharan, D. C. Jean, M. Liu, W. Yu, P. W. Baas, Tau does not stabilize axonal microtubules but rather enables them to have long labile domains. *Curr. Biol.* **28**, 2181–2189.e4 (2018).
2. H. Cho, J. Y. Choi, H. S. Lee, J. H. Lee, Y. H. Ryu, M. S. Lee, C. R. Jack Jr., C. H. Lyoo, Progressive tau accumulation in Alzheimer disease: 2-year follow-up study. *J. Nucl. Med.* **60**, 1611–1621 (2019).
3. K. Iqbal, F. Liu, C. X. Gong, I. Grundke-Iqbal, Tau in Alzheimer disease and related tauopathies. *Curr. Alzheimer Res.* **7**, 656–664 (2010).
4. H. Watanabe, E. Bagarinao, T. Yokoi, H. Yamaguchi, S. Ishigaki, M. Mausuda, M. Katsuno, G. Sobue, Tau accumulation and network breakdown in Alzheimer's disease. *Adv. Exp. Med. Biol.* **1184**, 231–240 (2019).
5. A. de Calignon, M. Polydoro, M. Suárez-Calvet, C. William, D. H. Adamowicz, K. J. Kopeikina, R. Pitstick, N. Sahara, K. H. Ashe, G. A. Carlson, T. L. Spires-Jones, B. T. Hyman, Propagation of tau pathology in a model of early Alzheimer's disease. *Neuron* **73**, 685–697 (2012).
6. C. A. Lasagna-Reeves, D. L. Castillo-Carranza, U. Sengupta, J. Sarmiento, J. Troncoso, G. R. Jackson, R. Kayed, Identification of oligomers at early stages of tau aggregation in Alzheimer's disease. *FASEB J.* **26**, 1946–1959 (2012).
7. Y. Yoshiyama, M. Higuchi, B. Zhang, S.-M. Huang, N. Iwata, T. C. Saido, J. Maeda, T. Suhara, J. Q. Trojanowski, V. M.-Y. Lee, Synapse loss and microglial activation precede tangles in a P301S tauopathy mouse model. *Neuron* **53**, 337–351 (2007).
8. P. Lei, S. Ayton, D. I. Finkelstein, L. Spoerri, G. D. Ciccotosto, D. K. Wright, B. X. W. Wong, P. A. Adlard, R. A. Cherny, L. Q. Lam, B. R. Roberts, I. Volitakis, G. F. Egan, C. A. McLean, R. Cappai, J. A. Duce, A. I. Bush, Tau deficiency induces parkinsonism with dementia by impairing APP-mediated iron export. *Nat. Med.* **18**, 291–295 (2012).
9. Z. Li, A. M. Hall, M. Kelinske, E. D. Roberson, Seizure resistance without parkinsonism in aged mice after tau reduction. *Neurobiol. Aging* **35**, 2617–2624 (2014).
10. N. Myeku, C. L. Clelland, S. Emrani, N. V. Kukushkin, W. H. Yu, A. L. Goldberg, K. E. Duff, Tau-driven 26S proteasome impairment and cognitive dysfunction can be prevented early in disease by activating cAMP-PKA signaling. *Nat. Med.* **22**, 46–53 (2016).
11. M. Catarina Silva, G. A. Nandi, S. Tentarelli, I. K. Gurrell, T. Jamier, D. Lucente, B. C. Dickerson, D. G. Brown, N. J. Brandon, S. J. Haggarty, Prolonged tau clearance and stress vulnerability rescue by pharmacological activation of autophagy in tauopathy neurons. *Nat. Commun.* **11**, 3258 (2020).
12. C. A. Lasagna-Reeves, M. de Haro, S. Hao, J. Park, M. W. C. Rousseaux, I. Al-Ramahi, P. Jafar-Nejad, L. Vilanova-Velez, L. See, A. De Maio, L. Nitschke, Z. Wu, J. C. Troncoso, T. F. Westbrook, J. Tang, J. Botas, H. Y. Zoghbi, Reduction of Nuak1 decreases tau and reverses phenotypes in a tauopathy mouse model. *Neuron* **92**, 407–418 (2016).
13. S. L. DeVos, R. L. Miller, K. M. Schoch, B. B. Holmes, C. S. Kebodeaux, A. J. Wegener, G. Chen, T. Shen, H. Tran, B. Nichols, T. A. Zanardi, H. B. Kordasiewicz, E. E. Swayze, C. F. Bennett, M. I. Diamond, T. M. Miller, Tau reduction prevents neuronal loss and reverses pathological tau deposition and seeding in mice with tauopathy. *Sci. Transl. Med.* **9**, eaag0481 (2017).
14. E. P. Spana, C. Q. Doe, Numb antagonizes notch signaling to specify sibling neuron cell fates. *Neuron* **17**, 21–26 (1996).
15. M. A. McGill, C. J. McGlade, Mammalian numb proteins promote Notch1 receptor ubiquitination and degradation of the Notch1 intracellular domain. *J. Biol. Chem.* **278**, 23196–23203 (2003).
16. J. Nie, M. A. McGill, M. Dermer, S. E. Dho, C. D. Wolting, C. J. McGlade, LNX functions as a RING type E3 ubiquitin ligase that targets the cell fate determinant Numb for ubiquitin-dependent degradation. *EMBO J.* **21**, 93–102 (2002).
17. M. Cayouette, M. Raff, Asymmetric segregation of Numb: A mechanism for neural specification from Drosophila to mammals. *Nat. Neurosci.* **5**, 1265–1269 (2002).
18. P. Zhou, J. Alfaro, E. H. Chang, X. Zhao, M. Porcionatto, R. A. Segal, Numb links extracellular cues to intracellular polarity machinery to promote chemotaxis. *Dev. Cell* **20**, 610–622 (2011).
19. E. J. Huang, H. Li, A. A. Tang, A. K. Wiggins, R. L. Neve, W. Zhong, L. Y. Jan, Y. N. Jan, Targeted deletion of numb and numblike in sensory neurons reveals their essential functions in axon arborization. *Genes Dev.* **19**, 138–151 (2005).
20. T. Nishimura, Y. Fukata, K. Kato, T. Yamaguchi, Y. Matsuura, H. Kamiguchi, K. Kaibuchi, CRMP-2 regulates polarized Numb-mediated endocytosis for axon growth. *Nat. Cell Biol.* **5**, 819–826 (2003).
21. J. Ferent, F. Giguère, C. Jolicoeur, S. Morin, J.-F. Michaud, S. Makihara, P. T. Yam, M. Cayouette, F. Charron, Boc acts via numb as a Shh-dependent endocytic platform for Ptch1 internalization and Shh-mediated axon guidance. *Neuron* **102**, 1157–1171.e5 (2019).
22. D. Ntelios, B. Berninger, G. Tzimagiorgis, Numb and Alzheimer's disease: The current picture. *Front. Neurosci.* **6**, 145 (2012).
23. C. C. Yap, B. Winckler, Adapting for endocytosis: Roles for endocytic sorting adaptors in directing neural development. *Front. Cell. Neurosci.* **9**, 119 (2015).
24. S. Chigurupati, M. Madan, E. Okun, Z. Wei, J. V. Pattisapu, M. R. Mughal, M. P. Mattson, S. L. Chan, Evidence for altered Numb isoform levels in Alzheimer's disease patients and a triple transgenic mouse model. *J. Alzheimers Dis.* **24**, 349–361 (2011).
25. A. Ashok, N. Singh, S. Chaudhary, V. Bellamkonda, A. E. Kritikos, A. S. Wise, N. Rana, D. M. Donald, R. Ayyagari, Retinal degeneration and Alzheimer's disease: An evolving link. *Int. J. Mol. Sci.* **21**, 7290 (2020).
26. N. J. Hart, Y. Koronyo, K. L. Black, M. Koronyo-Hamaoui, Ocular indicators of Alzheimer's: Exploring disease in the retina. *Acta Neuropathol.* **132**, 767–787 (2016).
27. W. L. Ho, Y. Leung, S. S. Y. Cheng, C. K. M. Lok, Y.-S. Ho, L. Baum, X. Yang, K. Chiu, R. C.-C. Chang, Investigating degeneration of the retina in young and aged tau P301L mice. *Life Sci.* **124**, 16–23 (2015).
28. A. London, I. Benhar, M. Schwartz, The retina as a window to the brain—FXro eye research to CNS disorders. *Nat. Rev. Neurol.* **9**, 44–53 (2013).
29. N. D. Bull, A. Guidi, M. Goedert, K. R. Martin, M. G. Spillantini, Reduced axonal transport and increased excitotoxic retinal ganglion cell degeneration in mice transgenic for human mutant P301S tau. *PLOS ONE* **7**, e34724 (2012).
30. L. Gasparini, R. A. Crowther, K. R. Martin, N. Berg, M. Coleman, M. Goedert, M. G. Spillantini, Tau inclusions in retinal ganglion cells of human P301S tau transgenic mice: Effects on axonal viability. *Neurobiol. Aging* **32**, 419–433 (2011).
31. M. Chiasseu, L. Alarcon-Martinez, N. Belforte, H. Quintero, F. Dotigny, L. Destroismaisons, C. V. Velde, F. Panayi, C. Louis, A. D. Polo, Tau accumulation in the retina promotes early neuronal dysfunction and precedes brain pathology in a mouse model of Alzheimer's disease. *Mol. Neurodegener.* **12**, 58 (2017).
32. V. Ramamurthy, C. Jolicoeur, D. Koutroumbas, J. Mühlhans, Y.-Z. Le, W. W. Hauswirth, A. Giessl, M. Cayouette, Numb regulates the polarized delivery of cyclic nucleotide-gated ion channels in rod photoreceptor cilia. *J. Neurosci.* **34**, 13976–13987 (2014).
33. A. Kechad, C. Jolicoeur, A. Tufford, P. Mattar, R. W. Y. Chow, W. A. Harris, M. Cayouette, Numb is required for the production of terminal asymmetric cell divisions in the developing mouse retina. *J. Neurosci.* **32**, 17197–17210 (2012).
34. S. Srinivas, T. Watanabe, C. S. Lin, C. M. William, Y. Tanabe, T. M. Jessell, F. Costantini, Cre reporter strains produced by targeted insertion of EYFP and ECFP into the ROSA26 locus. *BMC Dev. Biol.* **1**, 4 (2001).
35. O. Zilian, C. Saner, L. Hagedorn, H. Y. Lee, E. Säuberli, U. Suter, L. Sommer, M. Aguet, Multiple roles of mouse Numb in tuning developmental cell fates. *Curr. Biol.* **11**, 494–501 (2001).

36. P. H. Petersen, K. Zou, S. Krauss, W. Zhong, Continuing role for mouse numb and numbl in maintaining progenitor cells during cortical neurogenesis. *Nat. Neurosci.* **7**, 803–811 (2004).
37. A. Wilson, D. L. Ardiet, C. Saner, N. Vilain, F. Beermann, M. Aguet, H. R. MacDonald, O. Zilian, Normal hemopoiesis and lymphopoiesis in the combined absence of numb and numblike. *J. Immunol.* **178**, 6746–6751 (2007).
38. R. Bejarano-Escobar, G. Álvarez-Hernán, R. Morona, A. González, G. Martín-Partido, J. Francisco-Morcillo, Expression and function of the LIM-homeodomain transcription factor Islet-1 in the developing and mature vertebrate retina. *Exp. Eye Res.* **138**, 22–31 (2015).
39. J. Danias, K. C. Lee, M. F. Zamora, B. Chen, F. Shen, T. Filippopoulos, Y. Su, D. Goldblum, S. M. Podos, T. Mittag, Quantitative analysis of retinal ganglion cell (RGC) loss in aging DBA/2NNia glaucomatous mice: Comparison with RGC loss in aging C57/BL6 mice. *Invest. Ophthalmol. Vis. Sci.* **44**, 5151–5162 (2003).
40. M. A. Samuel, Y. Zhang, M. Meister, J. R. Sanes, Age-related alterations in neurons of the mouse retina. *J. Neurosci.* **31**, 16033–16044 (2011).
41. T. Koike, Y. Yang, K. Suzuki, X. Zheng, Axon & dendrite degeneration: Its mechanisms and protective experimental paradigms. *Neurochem. Int.* **52**, 751–760 (2008).
42. L. Luo, D. D. O'Leary, Axon retraction and degeneration in development and disease. *Annu. Rev. Neurosci.* **28**, 127–156 (2005).
43. K. R. Martin, R. L. Klein, H. A. Quigley, Gene delivery to the eye using adeno-associated viral vectors. *Methods* **28**, 267–275 (2002).
44. W. Hu, Y. Shu, Axonal bleb recording. *Neurosci. Bull.* **28**, 342–350 (2012).
45. A. Kneynsberg, B. Combs, K. Christensen, G. Morfini, N. M. Kanaan, Axonal degeneration in Tauopathies: Disease relevance and underlying mechanisms. *Front. Neurosci.* **11**, 572 (2017).
46. B. K. Fahrenthold, K. A. Fernandes, R. T. Libby, Assessment of intrinsic and extrinsic signaling pathway in excitotoxic retinal ganglion cell death. *Sci. Rep.* **8**, 4641 (2018).
47. T. T. Lam, A. S. Abler, J. M. Kwong, M. O. Tso, N-methyl-D-aspartate (NMDA)--induced apoptosis in rat retina. *Invest. Ophthalmol. Vis. Sci.* **40**, 2391–2397 (1999).
48. M. Morris, S. Maeda, K. Vossel, L. Mucke, The many faces of tau. *Neuron* **70**, 410–426 (2011).
49. J. Ericson, S. Thor, T. Edlund, T. M. Jessell, T. Yamada, Early stages of motor neuron differentiation revealed by expression of homeobox gene Islet-1. *Science* **256**, 1555–1560 (1992).
50. S. L. Pfaff, M. Mendelsohn, C. L. Stewart, T. Edlund, T. M. Jessell, Requirement for LIM homeobox gene Isl1 in motor neuron generation reveals a motor neuron-dependent step in interneuron differentiation. *Cell* **84**, 309–320 (1996).
51. T. Tsuchida, M. Ensini, S. B. Morton, M. Baldassare, T. Edlund, T. M. Jessell, S. L. Pfaff, Topographic organization of embryonic motor neurons defined by expression of LIM homeobox genes. *Cell* **79**, 957–970 (1994).
52. B. Allen, E. Ingram, M. Takao, M. J. Smith, R. Jakes, K. Virdee, H. Yoshida, M. Holzer, M. Craxton, P. C. Emson, C. Atzori, A. Migheli, R. A. Crowther, B. Ghetti, M. G. Spillantini, M. Goedert, Abundant tau filaments and nonapoptotic neurodegeneration in transgenic mice expressing human P301S tau protein. *J. Neurosci.* **22**, 9340–9351 (2002).
53. J. Bruch, H. Xu, T. W. Rösler, A. de Andrade, P. H. Kuhn, S. F. Lichtenthaler, T. Arzberger, K. F. Winklhofer, U. Müller, G. U. Höglinger, PERK activation mitigates tau pathology in vitroandin vivo. *EMBO Mol. Med.* **9**, 371–384 (2017).
54. M. L. Scattoni, L. Gasparini, E. Alleva, M. Goedert, G. Calamandrei, M. G. Spillantini, Early behavioural markers of disease in P301S tau transgenic mice. *Behav. Brain Res.* **208**, 250–257 (2010).
55. Z. Yin, F. Valkenburg, B. E. Hornix, I. Mantingh-Otter, X. Zhou, M. Mari, F. Reggiori, D. van Dam, B. J. L. Eggen, P. P. de Deyn, E. Boddeke, Progressive motor deficit is mediated by the denervation of neuromuscular junctions and axonal degeneration in transgenic mice expressing mutant (P301S) Tau protein. *J. Alzheimers Dis.* **60**, S41–S57 (2017).
56. P. Lei, S. Ayton, S. Moon, Q. Zhang, I. Volitakis, D. I. Finkelstein, A. I. Bush, Motor and cognitive deficits in aged tau knockout mice in two background strains. *Mol. Neurodegener.* **9**, 29 (2014).
57. J. W. Zhu, Y. F. Li, Z. T. Wang, W. Q. Jia, R. X. Xu, Toll-like receptor 4 deficiency impairs motor coordination. *Front. Neurosci.* **10**, 33 (2016).
58. C. J. Miedel, J. M. Patton, A. N. Miedel, E. S. Miedel, J. M. Levenson, Assessment of spontaneous alternation, novel object recognition and limb clasping in transgenic mouse models of amyloid-beta and tau neuropathology. *J. Vis. Exp.* 55523 (2017).
59. M. J. Lee, J. H. Lee, D. C. Rubinsztein, Tau degradation: The ubiquitin-proteasome system versus the autophagy-lysosome system. *Prog. Neurobiol.* **105**, 49–59 (2013).
60. N. V. Gorantla, S. Chinnathambi, Autophagic pathways to clear the Tau aggregates in Alzheimer's disease. *Cell. Mol. Neurobiol.* **41**, 1175–1181 (2020).
61. H. Sun, Y. Liu, L. Zhang, X. Shao, K. Liu, Z. Ding, X. Liu, C. Jiang, H. Li, H. Li, Numb positively regulates autophagic flux via regulating lysosomal function. *Biochem. Biophys. Res. Commun.* **491**, 780–786 (2017).
62. I. Tanida, T. Ueno, E. Kominami, LC3 and autophagy. *Methods Mol. Biol.* **445**, 77–88 (2008).
63. S. Jiang, K. Bhaskar, Degradation and transmission of tau by autophagic-endolysosomal networks and potential therapeutic targets for Tauopathy. *Front. Mol. Neurosci.* **13**, 586731 (2020).
64. C. Pernegre, A. Duquette, N. Leclerc, Tau secretion: Good and bad for neurons. *Front. Neurosci.* **13**, 649 (2019).
65. A. Grimaldi, C. Brighi, G. Peruzzi, D. Ragozzino, V. Bonanni, C. Limatola, G. Ruocco, S. di Angelantonio, Inflammation, neurodegeneration and protein aggregation in the retina as ocular biomarkers for Alzheimer's disease in the 3xTg-AD mouse model. *Cell Death Dis.* **9**, 685 (2018).
66. P. Marinković, S. Blumenstock, P. M. Goltstein, V. Korzhova, F. Peters, A. Knebl, J. Herms, In vivo imaging reveals reduced activity of neuronal circuits in a mouse tauopathy model. *Brain* **142**, 1051–1062 (2019).
67. C. Mason, N. Slavi, Retinal ganglion cell axon wiring establishing the binocular circuit. *Annu. Rev. Vis. Sci.* **6**, 215–236 (2020).
68. M. W. Fox, The visual cliff test for the study of visual depth perception in the mouse. *Anim. Behav.* **13**, 232–233 (1965).
69. N. Mazzaro, E. Barini, M. G. Spillantini, M. Goedert, P. Medini, L. Gasparini, Tau-driven neuronal and neurotrophic dysfunction in a mouse model of early Tauopathy. *J. Neurosci.* **36**, 2086–2100 (2016).
70. W. Zhong, M. M. Jiang, M. D. Schonemann, J. J. Meneses, R. A. Pedersen, L. Y. Jan, Y. N. Jan, Mouse numb is an essential gene involved in cortical neurogenesis. *Proc. Natl. Acad. Sci. U.S.A.* **97**, 6844–6849 (2000).
71. O. Bogdanović, M. Delfino-Machín, M. Nicolás-Pérez, M. P. Gavilán, I. Gago-Rodrigues, A. Fernández-Miñán, C. Lillo, R. M. Ríos, J. Wittbrodt, J. R. Martínez-Morales, Numb/Numbl-Opo antagonism controls retinal epithelium morphogenesis by regulating integrin endocytosis. *Dev. Cell* **23**, 782–795 (2012).
72. M. C. Belanger, B. Robert, M. Cayouette, Msx1-positive progenitors in the retinal ciliary margin give rise to both neural and non-neural progenies in mammals. *Dev. Cell* **40**, 137–150 (2017).
73. M. Hirai, Y. Arita, C. J. McGlade, K. F. Lee, J. Chen, S. M. Evans, Adaptor proteins NUMB and NUMBL promote cell cycle withdrawal by targeting ERBB2 for degradation. *J. Clin. Invest.* **127**, 569–582 (2017).
74. B. Combs, R. L. Mueller, G. Morfini, S. T. Brady, N. M. Kanaan, Tau and axonal transport misregulation in Tauopathies. *Adv. Exp. Med. Biol.* **1184**, 81–95 (2019).
75. M. Dubey, P. Chaudhury, H. Kabiru, T. B. Shea, Tau inhibits anterograde axonal transport and perturbs stability in growing axonal neurites in part by displacing kinesin cargo: Neurofilaments attenuate tau-mediated neurite instability. *Cell Motil. Cytoskeleton* **65**, 89–99 (2008).
76. J. E. Gerson, U. Sengupta, C. A. Lasagna-Reeves, M. J. Guerrero-Muñoz, J. Troncoso, R. Kayed, Characterization of tau oligomeric seeds in progressive supranuclear palsy. *Acta Neuropathol. Commun.* **2**, 73 (2014).
77. K. R. Patterson, S. M. Ward, B. Combs, K. Voss, N. M. Kanaan, G. Morfini, S. T. Brady, T. C. Gamblin, L. I. Binder, Heat shock protein 70 prevents both tau aggregation and the inhibitory effects of preexisting tau aggregates on fast axonal transport. *Biochemistry* **50**, 10300–10310 (2011).
78. S. Kang, S. M. Son, S. H. Baik, J. Yang, I. Mook-Jung, Autophagy-mediated secretory pathway is responsible for both normal and pathological Tau in neurons. *J. Alzheimers Dis.* **70**, 667–680 (2019).
79. Y. Wang, V. Balaji, S. Kaniyappan, L. Krüger, S. Irsen, K. Tepper, R. R. Chandupatla, W. Maetzler, A. Schneider, E. Mandelkow, E. M. Mandelkow, The release and trans-synaptic transmission of Tau via exosomes. *Mol. Neurodegener.* **12**, 5 (2017).
80. Y. Xu, S. Du, J. A. Marsh, K. Horie, C. Sato, A. Ballabio, C. M. Karch, D. M. Holtzman, H. Zheng, TFEB regulates lysosomal exocytosis of tau and its loss of function exacerbates tau pathology and spreading. *Mol. Psychiatry* **26**, 5925–5939 (2020).
81. G. A. Kyriazis, Z. Wei, M. Vandermey, D. G. Jo, O. Xin, M. P. Mattson, S. L. Chan, Numb endocytic adapter proteins regulate the transport and processing of the amyloid precursor protein in an isoform-dependent manner: Implications for Alzheimer disease pathogenesis. *J. Biol. Chem.* **283**, 25492–25502 (2008).
82. J. C. Grieger, V. W. Choi, R. J. Samulski, Production and characterization of adeno-associated viral vectors. *Nat. Protoc.* **1**, 1412–1428 (2006).
83. C. Aurnhammer, M. Haase, N. Muether, M. Hausl, C. Rauschhuber, I. Huber, H. Nitschko, U. Busch, A. Sing, A. Ehrhardt, A. Baiker, Universal real-time PCR for the detection and quantification of adeno-associated virus serotype 2-derived inverted terminal repeat sequences. *Hum. Gene Ther. Methods* **23**, 18–28 (2012).
84. T. Matsuda, C. L. Cepko, Electroporation and RNA interference in the rodent retina in vivo and in vitro. *Proc. Natl. Acad. Sci. U.S.A.* **101**, 16–22 (2004).
85. M. Cayouette, C. Gravel, Adenovirus-mediated gene transfer to retinal ganglion cells. *Invest. Ophthalmol. Vis. Sci.* **37**, 2022–2028 (1996).
86. F. D. W. Radstake, E. A. L. Raaijmakers, R. Luttge, S. Zinger, J. P. Frimat, CALIMA: The semi-automated open-source calcium imaging analyzer. *Comput. Methods Programs Biomed.* **179**, 104991 (2019).

Acknowledgments: We thank the IRCM core facilities for technical assistance, particularly J. Barthe for mouse colony management, D. Filion for help with microscopy and MATLAB analysis, E. Massicotte and J. Lord for help with flow cytometry, and S. Terrouz for hematoxylin/eosin colorations. We thank N. Stifani and B. Boulan for help with ImageJ plugin used for cell quantifications, N. Leclerc and A. Desjardins for the Tau::Flag and Tau::EGFP constructs, and C. A. Lasagna-Reeves and H. Y. Zoghbi for the DAOY cells. We are also grateful to all members of the Cayouette laboratory, past and present, for ongoing suggestions on this work. **Funding:** This study was supported by grants from the Alzheimer Society of Canada and the Canadian Institutes of Health Research (FDN-159936) to M.C. and LabEx LIFESENSES (ANR-10-LABX-65) and IHU FOReSIGHT (ANR-18-IAHU-01) to D.D. M.L. and S.C.H. were supported by IRCM Foundation fellowships, and M.C. is an Emeritus Research Scholar from the Fonds de recherche du Québec Santé (FRQS) and holds the Gaëtane and Roland Pillenière Chair in Retina Biology from the IRCM Foundation. **Author contributions:** Conceptualization: M.L. and M.C. Experimentation and data analysis: M.L., S.C.H., T.W.B., C.J., K.S., J.C., and T.B. AAV virus production: M.D. and D.D. Manuscript writing and editing: M.L. and M.C. Supervision and funding: M.C. **Competing interests:** M.C. and M.L. are inventors on a patent application related to this work filed by Adaerata LP (no. US17/309,425, filed 26 May 2019, published 03 February 2022). The authors declare that they have no other competing interests. **Data and materials availability:** All data needed to evaluate the conclusions in the paper are present in the paper and/or the Supplementary Materials. The DAOY cells can be provided by H. Y. Zoghbi pending scientific review and a completed material transfer agreement. Requests for the Daoy cells should be submitted to Baylor College of Medicine. The 3xTg mouse line, also known as B6.Cg-Psen1tm1Mpm Tg(APPSwe,tauP301L)1Lfa/J, can be provided by the Jackson laboratory pending scientific review and a completed material transfer agreement. Requests for the B6.Cg-Psen1tm1Mpm Tg(APPSwe,tauP301L)1Lfa/J should be submitted to F. LaFerla, University of California, Irvine, assigned strain ID 008880.

Submitted 16 September 2021
Accepted 7 September 2022
Published 19 October 2022
10.1126/sciadv.abm4295